Investigation of Ligand-Surface Interactions in Perovskite Nanomaterials using Solid-State NMR Spectroscopy and Density Functional Theory

MS Thesis

Submitted to

Indian Institute of Science Education and Research, Pune, in partial fulfilment of the requirements for the BS-MS Dual Degree Programme

By

Ankan Nath

Department of Physics

Indian Institute of Science Education and Research, Pune

Dr. Homi Bhabha Road,

Pashan, Pune 411008, INDIA

October 2024

Supervisor: Dr. Gaël de Paëpe, CEA Grenoble, France

Co-supervisor: Dr. Prasenjit Ghosh, IISER Pune, India

CERTIFICATE

This is to certify that this dissertation entitled “Investigation of Ligand-Surface Interactions in Perovskite Nanomaterials using Solid-State NMR Spectroscopy and Density Functional Theory” towards the partial fulfilment of the BS-MS dual degree programme at the Indian Institute of Science Education and Research, Pune represents study/work carried out by Ankan Nath at CEA Grenoble, under the supervision of Dr. Gaël de Paëpe, Group Leader, Modeling and Exploration of Materials Laboratory, and IISER Pune, under the supervision of Dr. Prasenjit Ghosh, Professor, Department of Physics, during the academic year 2024.

Ankan Nath

Committee:

Dr. Gaël de Paëpe

Dr. Prasenjit Ghosh

Prof. Angshuman Nag

DECLARATION

I hereby declare that the matter embodied in the report entitled “Investigation of Ligand-Surface Interactions in Perovskite Nanomaterials using Solid-State NMR Spectroscopy and Density Functional Theory” are the results of the work carried out by me at the Modeling and Exploration of Materials Laboratory, CEA Grenoble, under the supervision of Dr. Gaël de Paëpe, and the Department of Physics, IISER Pune, under the supervision of Dr. Prasenjit Ghosh, and the same has not been submitted elsewhere for any other degree. Wherever others contribute, every effort is made to indicate this clearly, with due reference to the literature and acknowledgement of collaborative research and discussions.

Ankan Nath, Roll No.: 20191118

ACKNOWLEDGEMENTS

I would like to thank my supervisors for not only helping me to formulate and solve the research problem, but also training me in techniques, both experimental and computational, that I had no experience with beforehand. I am grateful to all my lab members who have been very supportive and helpful throughout my project, both inside and outside the laboratory. I would also like to thank CEA for providing the funding for my stay. Finally, I would like to thank my friends and family for their support.

TABLE OF CONTENTS

List of Tables

List of Figures

ABSTRACT

Lead halide perovskites such as $CsPbBr_3$ in the form of colloidal nanocrystals possess amenable electronic and optical properties that find a wide variety of applications in optoelectronics and catalysis. However, the susceptibility of such nanocrystals towards surface defect formation during purification adversely affects their photochemical properties. A common strategy to overcome this problem is the use of long-chain charged organic ligands such as amines, carboxylates, and phosphonates for surface passivation. In spite of intense ongoing research focused towards understanding ligand binding on nanocrystal surfaces using techniques such as photoluminescence spectroscopy, infrared spectroscopy, and solution state nuclear magnetic resonance (NMR) spectroscopy, an experimentally determined atomic-level description of the ligand-binding mechanism on the perovskite surface sites still does not exist. In this project, we have aimed to characterize ligand-surface interactions on $CsPbBr_3$ nanocrystals at the atomic level using dynamic nuclear polarization (DNP) enhanced solid-state NMR complemented by density functional theory (DFT) calculations. From ^{1}H-^{13}C CP-HETCOR and ^{13}C-^{15}N TEDOR experiments, we have obtained the first reported experimental evidence of one-on-one cooperative interactions between the ammonium and carboxylate functional groups of the ligands, characterized by interaction distances of 3 – 6 Å obtained by spin dynamics simulations. 3D ^{13}C-^{15}N TEDOR experiments exhibit at least three distinct carboxylate environments and two distinct ammonium environments, signifying multiple conformations and binding modes. We have analyzed the ^{15}N and ^{13}C NMR spectra of the ligand functional groups by ab-initio chemical shift calculations of adsorption and substitution modes of ligand interaction with the different available nanocrystal facets. The computed binding energies for the different binding modes show that Cs substitution by the ammonium functional group of the protonated amine ligand is the most favored. DFT-calculated chemical shifts for such conformations correlate with the NMR spectra at low temperature. Co-substitution studies of the two types of ligands also support the TEDOR analysis. The results of this project provided much needed clarity regarding ligand-surface interactions in perovskite nanocrystals that will be very helpful in ligand engineering aimed towards improving surface passivation of more environment-friendly perovskite nanomaterials, as well as enhancing nanocrystal properties for applications such as LEDs and photocatalysis.

INTRODUCTION

The discovery of the first metal halide perovskites in 1893 [1] opened the avenue to a class of semiconducting materials with intriguing opto-electronic properties such as enhanced charge transport [2], high color purity, and low nonradiative recombination rates [3]. It is no surprise that over time, metal halide perovskites have been used in a variety of applications. Perovskite solar cells have achieved power conversion efficiencies of more than 30% [4]. On the other hand, the amenable light emitting properties of metal halide perovskites have resulted in their employment in LEDs with high quantum efficiencies [5], as well as lasers with high coherence, low threshold, and multicolor tunability [6]. Metal halide perovskites have a typical chemical formula of ABX_3, where A and B are cations and X is a halogen. Structurally, they are composed of $[BX_6]^{4-}$ octahedra, with A^+ occupying the cuboctahedral sites coordinating with 12 X^- anions (Figure 1).

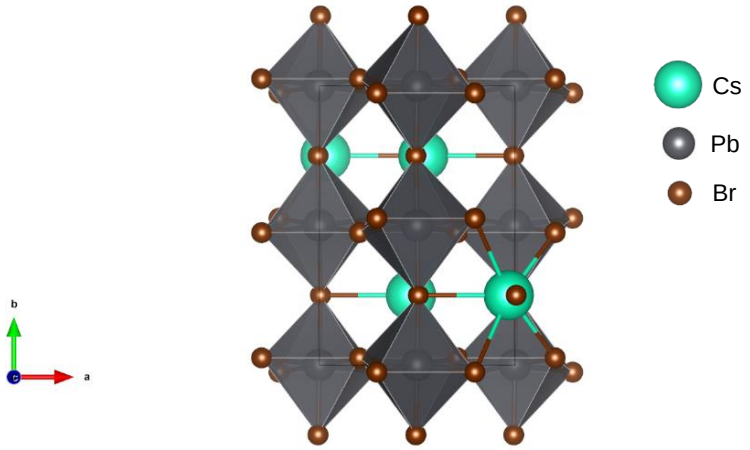

Figure 1: Bulk Crystal Structure of $CsPbBr_3$ (from [46])

Perovskites in the bulk material form have an inherently lower photoluminescence quantum yield (PLQY), which in important measure for the efficiency of optoelectronic materials. This is primarily because of two reasons: (i) the presence of mobile charged and neutral defects that can be stabilized by the ionic lattice and hence have a low formation energy, and (ii) low excitonic binding energies, resulting in decreased electron-hole capture translating to lowered radiative recombination. Thin films of perovskites synthesized from precursor solutions have been studied as alternatives, but intrinsic defects such as grain boundaries have been observed to affect their performance due to nonradiative losses [7]. Hence, focus was shifted to perovskite nanocrystals (PNCs) during the last decade.

(A) HISTORY OF PNC SYNTHESIS

The first colloidal synthesis of lead halide PNCs was reported in 2014 [8], where the preparation of highly stable colloidal solutions of 6 nm-sized $MAPbBr_3$ ($MA = CH_3NH_3^+$) NCs was demonstrated with a PLQY of 20%, compared to 16% for bulk perovskites [79]. A similar methodology was applied by Protesescu *et al.* in 2015 [9] for the synthesis of $CsPbX_3$ NCs (X = Cl, Br, I). The synthesis procedure, inspired from the standard hot-injection synthesis of classic colloidal quantum dots such as CdSe [10], involved reacting a Cs-precursor solution with a Pb-halide precursor solution in the presence of organic ligands to colloidally stabilize the NCs. The $CsPbX_3$ PNCs obtained were monodisperse, with a cubic morphology, and their size could be controlled in the range of 4-15 nm by tuning the reaction temperature from 140°C to 200°C. The halide stoichiometry could also be controlled by using appropriate halide ratios in the Pb-halide precursor solution, enabling the synthesis of mixed-halide PNCs. Although $CsPbX_3$ can crystallize in orthorhombic, tetragonal, and cubic lattices, only the cubic phase was obtained in this study due to the high reaction temperature as evidenced from the X-ray diffraction patterns.

In the hot-injection method, the primary factors that control the phase, morphology, size, and dispersity of the NCs are the following: (i) temperature for mixing of precursor solutions, (ii) concentration of precursor solutions, (iii) the ratio of stabilizing ligands to precursors, and (iv) the reaction time. Controlling (ii) and (iii) allowed for the synthesis of PNCs with alternative phases such as Cs_4PbX_6 and $CsPb_2Br_5$ [11, 12], while controlling (i), (iii) and (iv) resulted in the formation of perovskite nanowires and nanosheets [13, 14].

The traditional two-precursor hot-injection method does not allow control over the Pb^{2+}-halide ratio due to the use of a single lead halide precursor solution, thus making an avenue of stoichiometry control inaccessible. As a solution, Liu *et al.* developed the "three-precursor" hot-injection method in 2017 for $CsPbX_3$ PNC synthesis [15] by using NH_4X and PbO as anionic and cationic precursors separately instead of a single PbX_2 precursor, resulting in PNCs with improved optical properties and stability. The three-precursor hot-injection method has been optimized by using alternative halide precursors such as benzoyl halide [16] and silyl halide [17], enabling the synthesis of PNCs with a variety of different compositions.

The hot-injection protocol requires a complex chemical apparatus, thus making industrial production difficult. An alternative method for the synthesis $CsPbX_3$ PNCs was demonstrated by Li *et al.* in 2016 [18]. Termed as "ligand-assisted reprecipitation" or LARP, this method

uses the concept of supersaturated recrystallization to perform PNC synthesis at room temperature. As is a theme with every synthesis procedure, problems became apparent with the LARP method. There were difficulties in the solubilization of the cationic salts at room temperature as well as control over the growth mechanism. These were solved by Akkerman *et al.* in 2022 [19] by using trioctylphosphine oxide (TOPO) to solubilize Pb^{2+} and diisooctylphosphinate (DOPA) to solubilize Cs^{+}, allowing for the size-tunable synthesis of CsPbBr3 PNCs with a PLQY of ~90%.

A feature common to all the techniques mentioned is how simple and inexpensive the synthesis is, which has resulted in growing interest in PNCs, along with improving and modulating their properties, which will be discussed in the next section.

(B) PROPERTIES OF PNCs

The 2015 study by Protesescu *et al.* [9] reported that colloidally synthesized $CsPbBr_3$ PNCs had high PLQYs of 50-90% and low emission FWHMs of 12-42 nm. This indicates that these PNCs were monodisperse, which was also evidenced by transmission electron microscopy (TEM) images and X-ray diffraction patterns. In this first report, the photoluminescence decay times were in the range of 1-29 ns, which was improved in subsequent studies [20]. The emission spectra of these PNCs were tunable over the entire visible spectral region of 410-700 nm. This was possible due to control over the following two parameters:

(i) Halide composition: $CsPbCl_3$ PNCs showed emission at 410 nm while $CsPbI_3$ PNCs were on the other end at 700 nm. CsPbBr3 PNCs emitted at the intermediate wavelength region of ~500 nm. Mixed halide compositions such as Cl/Br and Br/I covered the rest of the visible spectrum from 400-500 nm and 500-750 nm respectively.

(ii) Nanocrystal size: For semiconductor nanocrystals whose dimensions are smaller than or similar to the natural delocalization lengths of an exciton in the bulk material, quantum confinement effects come into play, resulting in blue shift of the emission peak [21]. $CsPbBr_3$ PNCs with edge length below 10 nm showed significant quantum confinement effects in their band gap and emission peaks.

These amenable properties have led to the applications of colloidal PNCs in LEDs [9] as well as single-photon emission for quantum technologies.

Metal halide perovskites are defect tolerant semiconductors, which refers to their capability to maintain their electronic structure despite a high defect concentration. These perovskites possess mainly three kinds of defects, namely (i) interstitials, where either individual ions or ion pairs occupy interstitial sites within the structure, (ii) antisites, where a cation occupies an anionic lattice position or vice-versa, and (iii) vacancies, where either individual ions or ion pairs are missing from their natural sites. DFT studies have shown that these defects have a low formation energy in bulk perovskites due to stabilization by the ionic lattice, which can result in higher defect concentrations and imposing an upper limit on the PLQY [22].

Metal halide PNCs have a core-shell structure, i.e, they are composed of a core which is structurally and stoichiometrically equivalent to the bulk material, and a shell that is 2-3 atomic layers thick and interacting with the surfactants. This high surface-bulk ratio results in greater defect formation at the NC surface. Not all defects result in the formation of midgap trap states in the electronic structure which are responsible for lowering PLQY. DFT studies have shown that surface vacancies are an exception, as they can be easily formed during post-synthesis processing of PNCs and result in the formation of these aforementioned trap states [23]. Another important factor affecting the applicability of PNCs is their degradation in ambient conditions, due to the surface being sensitive to moisture, oxygen, and light [24]. Understanding the surface properties of PNCs is thus essential to improve their synthesis, processing, and performance.

(C) SURFACE CHEMISTRY OF PNCs

Metal halide PNCs such as those of $CsPbBr_3$ grow very fast in the hot-injection method. The reaction mixture must be quenched within 10 s [9]. This makes the study of the PNC growth mechanism very difficult. In spite of this, it has been correctly assumed that the surface energies of the different facets play a very important role in determining the directionality of PNC growth. This nuance has been demonstrated in computational studies which show how different the stabilities of the possible surface terminations are, in the range 0.069-0.220 Jm^{-2} [25]. Due to their highly ionic nature, the NCs that form initially can self-assemble and aggregate to form structures that are closer and closer to the bulk material. This aggregation is arrested by the surfactants used during synthesis.

$CsPbBr_3$ PNCs have CsBr and $PbBr_2$ terminations that can have vacancies which may be occupied by the functional groups of the ligands. The ligand-PNC interaction is expected to operate through the undercoordinated surface ions. This interaction is also responsible for the

degradation of PNCs in ambient conditions [26] and in polar solvents [27]. The active molecules such as moisture, oxygen, and solvents can decompose or pull ions from the PNC surface. This can have effects of varying severities, ranging from decrease in PLQY to complete loss of structural integrity, necessitating the use of surfactants to passivate the PNC surface.

A classification method to better understand ligand interactions in PNCs was introduced by De Roo *et al.* in 2016 [28] based on Covalent Bond Classification developed by Green [29] for metal-ligand interactions in inorganic complexes. By this protocol, ligands can be (i) L-type, which are Lewis bases that contribute 2 electrons to the NC-ligand bond, (ii) Z-type, which are Lewis acids that interact through an empty orbital, and (iii) X-type, which donate 1 electron to the NC-ligand bond. Each of these ligands show unique chemical reactions, resulting in a complex interface at NC surfaces as observed for covalent NCs [30]. The hot-injection synthesis of $CsPbBr_3$ NCs have used "native" ligands that are added during the reaction. These surfactants are responsible for dissolving the Cs and Pb salts, as well as stabilizing the PNC surface and halting their growth. As has been described in the previous sections, there are some surfactants such as oleic acid and oleylamine [9, 28] that are added during the hot-injection step. These are termed as "native" ligands as they are used during PNC synthesis. De Roo *et al.* observed that binding of native ligands to the PNC surface is highly dynamic with a high possibility of detachment during the purification step [28]. However, it is imperative to use primary amines and carboxylic acids as native ligands in the two-step hot-injection procedure in order to solubilize $PbBr_2$ which is the sole source of Br^-. The three-precursor hot-injection method allows modification of Br^- concentration in the reaction medium, which has enabled the testing of alternate surfactants as native ligands. These include secondary amines [31] which do not show an improvement in PLQY of the $CsPbBr_3$ PNCs, and more importantly phosphonic acids [32] that produce PNCs with a truncated octahedron shape, high stability, and high PLQY.

The dynamic binding of primary amines and carboxylic acids to $CsPbBr_3$ PNC surfaces has been exploited in post-synthesis modifications, where stronger binding surfactants are added during after the synthesis. These ligands can exchange with the native ligands, resulting in improved stability and PLQY of the final purified PNCs. Phosphonic acids have been a natural choice for ligand exchange [33]. Quaternary alkylammonium bromides have also shown similar improvements in PNC stability and PLQY [34]. However, the use of these charged, strongly-binding ligands can result in degradation of the PNC surface if used in excess due to

a multitude of reactions that are possible in the colloidal suspension. This has been solved using neutral zwitterionic ligands that can cap the PNC surface by binding to two different sites, imparting added stability without degradation of PNCs. The approach was introduced by Krieg *et al.* in 2018 [35] using cheap and common zwitterionic ligands such as sulfobetaines. Optimization of zwitterionic ligand headgroup and tail properties was performed in subsequent studies [36].

Through the last decade, ligand combinations have been used to improve PNC stability and performance. However, the approach has largely been brute-force. There have been attempts to understand and experimentally study the ligand-surface interactions, but the conclusions drawn have been either very indirect or indecisive.

(D) LIGAND-BINDING: TECHNIQUES AND INFERENCES

The optical performance of $CsPbBr_3$ PNCs, representing the quality of the synthesis and purification procedure, has been measured using absorbance and photoluminescence spectroscopy. However, insight into the mechanism of ligand-binding on the PNC surface is necessary to understand their stability. Structural characterization of the PNC is essential before looking at the ligands. X-ray diffraction (XRD) has proven a very suitable technique for this purpose, providing information not only about the phase and crystal lattice of the PNCs, but also their size [37] and dispersity [38] through XRD lineshape analysis.

An important structural aspect of PNCs that dictates their interaction with ligands is their surface termination, the determination of which is made possible through electron microscopy. Transmission electron microscopy (TEM) images provide information about the shape, size, and dispersity of the synthesized PNCs. High resolution TEM (HRTEM) further enables the observation of distances between lattice planes, and hence an idea of the Miller indices of the PNC surface terminations [39]. This indexing can be also confirmed by high-angle annular dark-field scanning transmission electron microscopy (HAADF-STEM) imaging and fast Fourier transform (FFT) analysis. In conjugation with simulated electron diffraction patterns, this can also be used to determine individual atomic positions [40]. Grazing incidence wide angle X-ray scattering (GIWAXS) is a complementary technique especially useful for understanding the growth mechanism of anisotropic nanostructures [39] by analyzing the reciprocal space patterns of the perpendicular and in-plane components of the scattering vector. In spite of the accuracy of TEM, conventional techniques cannot be used for metal halide PNCs since they are highly radiation-sensitive. For example, Pb^{2+} ions from $CsPbBr_3$ PNCs can be

reduced to Pb^0 atoms through a radiolysis process, which is followed by aggregation to form Pb nanoparticles [41]. This has proven to be misleading to studies investigating the growth mechanism of PNCs [42]. Thus, the experimental parameters such as electron dose rates have to be modified for TEM to be used for such PNCs [43].

TEM cannot be used to visualize the ligands on the PNC surface due to their orientational disorder and dynamic nature, necessitating the use of other techniques to study ligation. Identification of different ligand species has been achieved using Fourier transform infrared (FTIR) spectroscopy, through the assignment of vibrational modes specific to the ligand functional groups. This includes modes such as carboxylate asymmetric stretching and N-H bending vibrations [44, 45], which can be used to characterize not only the protonation states of the interacting ligands, but also the effect of PNC purification and washing on the integrity of the surface-ligand interface. FTIR analysis can be used to study not only native ligands, but also sulfonates and other ligands that can be used for exchange through their characteristic vibrational modes [45]. In most studies, FTIR spectroscopy is complemented with X-ray photoelectron spectroscopy (XPS). The PNCs can be probed in a depth-specific fashion by tuning the incident photon energies, allowing separation of elemental signatures from the surface and the bulk [46]. Another essential piece of structural information about the PNCs that can be extracted from XPS analysis is the elemental ratio, an indicator of the surface composition and extent of defects [47]. Ligand species on the PNC surface can also be identified by XPS, an example being the identification of amine binding modes through analysis of the N 1s region [47].

A drawback of the previously listed techniques is that they cannot be used to study PNCs in their native colloidal state, thus losing out on information about dynamics. Solution-state nuclear magnetic resonance (NMR) has been proven to be a powerful technique for the study of ligands on the PNC surface. NMR can be used to investigate both the static and dynamical properties of a system in a non-invasive and non-destructive fashion. The versatility of solution NMR has been demonstrated over a long period of time, especially in the case of colloidal quantum dots such as CdSe and PbSe [48], and was incorporated into the study of $CsPbBr_3$ PNCs by De Roo *et al.* [28]. The presence of oleic acid and oleylamine in the purified NC sample was inferred from the presence of characteristic alkene and aliphatic peaks in the ^1H NMR spectrum, which were used to quantify these ligands. Ligand dynamics were determined through the following techniques: (i) nuclear Overhauser effect spectroscopy (NOESY), which exploits the timescale of the ligand motion to distinguish between free and bound species, and

(ii) diffusion-ordered NMR spectroscopy (DOSY), which utilizes magnetic field gradients to determine the translational diffusion coefficient of each peak and hence determine the mobility of the ligand species. Further titration studies by addition of the amine ligand revealed the possibility of a ligand shell composed of both kinds of ligands (oleylamine and oleic acid) around the PNCs, which can exchange with the surface-bound ligands. Cooperativity between the ligands was suggested as a possible explanation for the ligand dynamics without providing a model or further evidence in this regard. Smock *et al.* expanded on the use of solution NMR [33] by showing that the alkenyl peak of oleic acid was a combination of signals from three species that have been termed free, physisorbed, and bound, based on the chemical shifts of these peaks relative to that from a reference oleic acid. Also, ligand exchange was performed by titration with longer chain carboxylic acids and amines, as well as phosphonic acid. This approach yielded equilibrium constants for ligand exchange, which was the first time the thermodynamics of this exchange mechanism were studied.

Despite all its advantages, solution NMR still cannot probe the exact mechanism of ligand-surface interactions, which is why the systems have been also studied computationally. DFT calculations have been performed on a series of possible ligand-surface interactions. Both neutral ligands [47] and their conjugate acids/bases [46] have been studied in this regard. The acids have been found to interact with the PNC surface through oxygen-cation bonds, while the amines passivate the surface through the formation of H-bonds between the ammonium protons and the surface Br atoms [49]. This passivation has also been shown to improve the defect tolerance of these systems. MD simulations have also been used to incorporate solvent effects into ligand binding [36].

Despite the wealth of information available from solution NMR and the other mentioned techniques, atomic level characterization of the PNC surface is still missing from the picture. This can be achieved only through solid-state NMR by exploiting the internal spin interactions using tailored NMR experiments. The implementation of solid-state NMR for PNCs is discussed in the next section.

(E) SURFACE CHARACTERIZATION: SOLID-STATE NMR

Solid-state NMR studies have been performed on dry powders of colloidally synthesized $CsPbBr_3$ PNCs [50]. Surface-specific NMR techniques provided a qualitative understanding of the PNCs. As a prerequisite, high NMR signal intensity is necessary for accurate atomistic characterization of the PNC-ligand interface. Signal enhancement techniques such as dynamic

nuclear polarization (DNP) have been used to solve this problem for the study of CdSe nanocrystals [51] and ZnO nanoplatelets [52]. The application of DNP to PNCs has proven to be difficult. One of the problems with perovskites is their tendency to aggregate, which hurts the DNP efficiency. An attempt to solve the aggregation problem was made in 2015 by homogeneously dispersing the sample in mesoporous silica [53]. Improvements were made in the implementation of DNP for perovskites by modifying the polarizing agents used and slowing the ^{1}H relaxation through deueteration. This approach was used for the study of hybrid organic-inorganic perovskite thin films [54]. Another way to increase DNP enhancement is impregnation DNP, where the sample is doped with high-spin metal ions such as Mn^{2+} which can enhance the signal of other nuclei in their proximity. Impregnation DNP was used to study μm-sized $CsPbCl_3$ crystals [55].

A problem that had hitherto not been addressed was the absorption of μwave radiation necessary for DNP (explained in "Materials and Methods" Section (D)) by the perovskites, which caused localized heating to an extent that phase transformations were induced within the material [55]. Also, heating effects decrease DNP efficiency by affecting the phase of the DNP matrix as well as speeding up ^{1}H relaxation. The heating problem has been solved by cooling down the system to 30 K with a homebuilt helium closed-cycle system developed in-house in Grenoble [56].

This study takes advantage of the state-of-the-art DNP system to understand and characterize the ligand-mediated passivation mechanism of colloidally synthesized $CsPbBr_3$ PNCs. More specifically, this study focuses on the experimental characterization of proximities between the ligands themselves as well as between the ligands and the surface through the use of surface-specific solid-state NMR techniques. Instead of attempting to improve the colloidal stability and PLQY of $CsPbBr_3$ PNCs with new synthesis and purification methods, this study endeavors to create a framework for atomic-level characterization of the surface-ligand interface of PNCs using a combination of solid-state NMR and DFT calculations. Such an experimental framework is essential for the intelligent design of new and improved colloidal PNCs.

MATERIALS AND METHODS

(A) MATERIALS

$CsPbBr_3$ NCs were prepared based on the hot-injection synthesis procedure described in [50]. The native ligands used were dodecylamine and oleic acid (Figure 2). Essentially, the Cs(oleate) precursor solution was injected into the $Pb(oleate)_2$ precursor solution (containing dodecylamine) at a high temperature to form the colloidal suspension of PNCs, which was cooled and purified by cycles of centrifugation and washing with polar solvents, followed by drying to prepare the solid-state NMR sample. Optimization of the injection temperature, and purification and drying protocols was performed beforehand, which is not included in this thesis. Powder X-ray diffraction and TEM was used to characterize the structure of the synthesized PNCs, which are also not a part of this study.

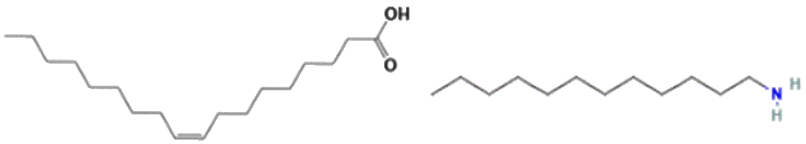

Figure 2: Native ligands used for synthesis, namely oleic acid (left) and dodecylamine (right)

Demonstration and calibration for the NMR experiments described in section (E) was performed with commonly used solid-state NMR standards such as commercially available natural abundance glycine and histidine. The f-MLF tripeptide sample was used from [56].

(B) AN INTRODUCTION TO SOLID-STATE NMR

In the basic high-field NMR experiment, an external magnetic field is applied to a sample which causes a net nuclear spin polarization along the applied field. This polarization can be brought into the transverse plane by the application of radiofrequency (RF) pulses. Once in the transverse plane, the nuclear spin polarization precesses under the external magnetic field, and this precession can be recorded by the induced voltage developed in a detector coil. The entire experiment takes place within an NMR probe placed in a strong superconducting electromagnet. This time-domain precession data, also known as a free induction decay (FID), is Fourier transformed to generate the frequency domain NMR spectrum. The spectrum is composed of peaks whose positions correspond to the angular frequency of precession of the nuclear spin polarization, which is unique to each of the distinct species present in the sample. The precession frequency is directly proportional to the gyromagnetic ratio of the nucleus,

which is a unique nuclear property, and the external magnetic field applied. Thus, the precession frequency can be used as a signature of the nuclei of interest in the sample as it depends on their immediate chemical environment. This signature is termed as the chemical shift of that nuclear signal.

Apart from the external interactions, namely the longitudinal magnetic field and RF pulses, there are a number of internal interactions in the spin system. The versatility of NMR lies in the ability to exploit these interactions using tailored RF pulses. These interactions have different magnitudes. Mathematically, the internal interactions are represented by tensors which can be decomposed into an isotropic part, which is uniform in all directions, and an anisotropic part, which is dependent on the orientation of that tensor's principal axis system (PAS) relative to the external magnetic field. The relevant interactions for our study have been summarized below:

(i) Chemical Shift: This arises from the interaction of the nucleus with the surrounding electron density due to the external magnetic field.

(ii) Dipole-dipole coupling: This represents the direct magnetic dipolar coupling between the interacting nuclear spins. The dipolar coupling interaction is purely anisotropic.

(iii) Quadrupolar coupling: This occurs in spin > ½ nuclei (such as ^{133}Cs and ^{207}Pb) due to their interaction with the field gradient of the surrounding electron density.

In solution NMR, the anisotropic part of each of these interactions averages out due to fast molecular tumbling, leaving only the isotropic part. The isotropic part of the chemical shift interaction gives rise to the NMR signature being discussed previously. The averaging of the anisotropic part results in very sharp and intense NMR signals in solution, but a drawback is that most of the information about the system is lost. The anisotropic interactions are retained in the solid-state, but solid-state NMR signals are broad due to the orientational distribution of the crystallites and hence the anisotropic interactions in the sample. The increased signal width decreases the signal-to-noise ratio, necessitating higher experimental times to obtain a good NMR spectrum. This led to the development of magic angle spinning (MAS) NMR in 1958 [57].

MAS-NMR utilizes the orientational dependence of the anisotropic interactions, which is generally proportional to the second order Legendre polynomial $\mathrm{P}_2(\cos\beta) = (3\cos^2\beta - 1)/2$, where β is the angle between the longitudinal axis of the interaction tensor and the

external magnetic field. This term vanishes for a particular β known as the 'magic angle', which is around 54.74º. It is not possible to align all the crystallites at this angle in a powder. However, the same averaging effect is achieved when the powder sample is spun around an axis oriented at the magic angle to the external magnetic field. The averaging of the anisotropic interactions occurs most effectively when the MAS rate is greater than or close to the magnitude of the anisotropic interaction. Otherwise, the broad static solid-state spectrum is split into a set of peaks known as spinning sidebands that are separated in the frequency dimension by the MAS frequency. MAS is achieved by packing the sample into a rotor, which is aligned at the magic angle to the longitudinal magnetic field. This rotor has fans on its cap, which are spun by a gas flow known as the 'drive'. The rotor is stabilized during free spinning by a gas flow called the 'bearing' (Figure 3). Smaller rotors can achieve higher MAS speeds.

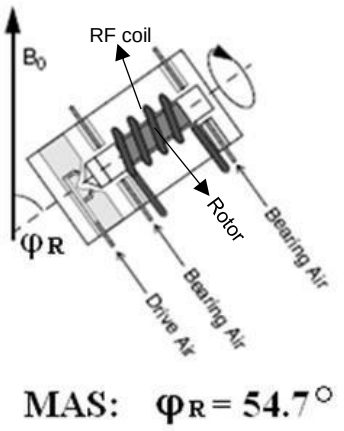

Figure 3: Schematic of MAS-NMR displaying all primary components

Both solution-state and MAS-NMR achieve sharp signals from the averaging of the anisotropic interactions. An important difference between the two is in terms of the ability to recover the information stored in the anisotropic interactions. In solution-state NMR, all the molecules tumble randomly, resulting in complete loss of this interaction information. However, in MAS-NMR, the averaging is due to the sample spinning which is at an uniform rate and hence periodic. This is very important in order to obtain interaction information. For example, the sideband pattern for lower MAS rates can be simulated theoretically to obtain the chemical shift anisotropy [58]. Also, pulse sequences can be tailored to be such that the spin system evolution recovers information about the interactions of choice.

(C) SPIN DYNAMICS SIMULATIONS IN SIMPSON

The evolution of the spin system throughout an NMR experiment, in the absence of relaxation and other dissipative processes, can be mathematically described using the Liouville-Von Neumann equation:

Equation 1

$$\frac{d}{dt}\rho(t) = -i[H(t), \rho(t)]$$

where $H(t)$ is the time-dependent Hamiltonian encapsulating both the external and internal interactions, and $\rho(t)]$ is the density matrix for the spin system.

The solution can be expressed as:

Equation 2

$$\rho(t) = U(t,0)\rho(0)U^*(t,0)$$

where $U(t,0)$ is the unitary cyclic propagator for the time period 0 to t. In terms of the Hamiltonian, the propagator is:

Equation 3

$$U(t,0) = \exp\left\{-i\int_0^t H(t')dt'\right\}$$

There are various analytical ways to evaluate the propagator, such as average Hamiltonian theory [58]. These provide good first order formulations which can be used to understand a range of different NMR experiments. However, higher order terms in these formulations and cross terms in between interactions become too complicated to evaluate analytically, especially after the inclusion of MAS. This necessitates the use for numerical methods to simulate all kinds of NMR experiments for any spin system and interaction sets.

SIMPSON [59] is a versatile and efficient software for spin dynamics simulations, which takes the spin system, set of interactions, MAS rate, and user-defined pulse sequence as input, and computes the FID through the following steps: (i) frame transformations of the interaction to crystallite, rotor, and laboratory frames using input Euler angles in between each frame, (ii) evaluation of the propagator in the laboratory frame by discretizing the integral, and (iii) average over a set of crystallites for all kinds of systems, both oriented crystals as well as powders. The generated FID can be further processed with inbuilt modules.

SIMPSON has been used to study a variety of different NMR experiments. The simulated datasets can be used in established Python fitting modules for the analysis of real experimental data. SIMPSON has been used for all the spin dynamics simulations in this study.

(D) DYNAMIC NUCLEAR POLARIZATION (DNP)

In NMR, the detected quantity is the nuclear spin polarization, which is developed initially by the application of an external magnetic field. Thus, the signal intensity is directly proportional to the amount of spin polarization that can be generated. This polarization is essentially the population difference between the nuclear spin levels due to the external magnetic field, which can be derived for a spin – ½ system under the high field approximation:

Equation 4

$$P = P_{+\frac{1}{2}} - P_{-\frac{1}{2}} = N\frac{e^{\frac{\hbar\gamma B_0}{2k_B T}} - e^{\frac{-\hbar\gamma B_0}{2k_B T}}}{2} \approx \frac{N\hbar\gamma B_0}{2k_B T}$$

The polarization hence is directly proportional to the number of NMR-active nuclear spins N, gyromagnetic ratio γ, the applied external magnetic field B_0, and inversely proportional to the temperature T. ^{1}H has the highest nuclear gyromagnetic ratio. Despite this, substituting standard values results in a net ^{1}H spin polarization less than 0.01%, which is representative of the low inherent sensitivity of NMR. Another important factor contributing to the sensitivity of NMR relates to N. For a particular element, not all isotopes are NMR-active, and the fraction of NMR-active isotopes is termed as the natural abundance. Some nuclei such as ^{1}H have a very high natural abundance (99.99%). The problem arises with nuclei such as ^{13}C and ^{15}N which have natural abundances of 1.1% and 0.36% respectively. Getting a good signal-to-noise ratio with these nuclei at natural abundance can require unfeasibly long experimental times. This problem can be solved partly by labelling, but it is an expensive process and not always feasible.

Dynamic nuclear polarization (DNP) has provided a way to enhance the low inherent sensitivity of NMR by utilizing the fact that electron spins can be polarized to a much greater extent compared to nuclei due to their higher gyromagnetic ratio [60]. The sample is impregnated with a polarizing agent, which are radicals possessing unpaired electrons at the paramagnetic centers. The electronic spin levels are saturated by a magnetic field, using microwave radiation generated by a gyrotron. This irradiation causes population transfer from electrons to the nuclei through the hyperfine interaction. In typical systems (including the

system in this study), the nuclei being polarized by DNP are ^{1}H's. The ^{1}H's close to the paramagnetic centers are polarized first, and this polarization spreads through the extended ^{1}H spin system in the DNP matrix through spin diffusion. This process finally results in polarizing the ^{1}H's in the sample of interest (Figure 4).

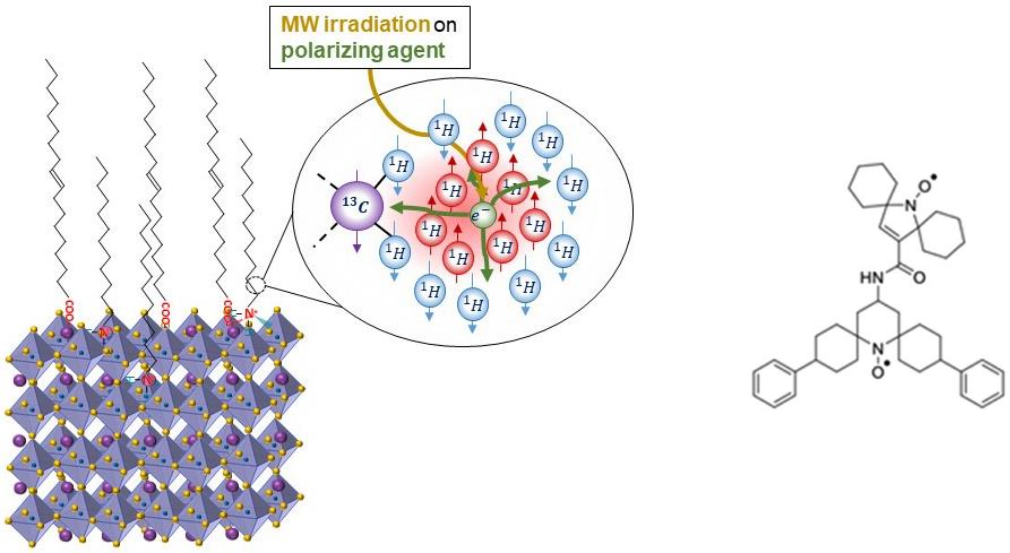

Figure 4: Schematic for the mechanism of DNP on PNCs (left) and structure of the polarizing agent cAsymPol-TEK (right). Polarization is transferred from the active red protons of the polarizing agent to the blue protons of the solvent and sample.

The maximum possible polarization enhancement that can be achieved through DNP is equal to γ_e/γ_n, which is around 658. However, this is not achieved due to competition with dissipative processes such as electronic and nuclear spin relaxation. Thus, the optimization of DNP enhancement under MAS has been a topic of immense interest [61]. There are multiple factors that contribute to the enhancement, such as (i) system temperature, which affects the relaxation rates, and microwave absorption by the phase of the DNP matrix, and (ii) the polarizing agent, in terms of the hyperfine interactions strengths responsible for DNP [85]. The optimization of the DNP system to achieve the highest sensitivities in a cost-effective fashion has been performed by the Grenoble group [56], achieving stable sample spinning even after cooling to 30 K. It is this system which has been used for the DNP-enhanced NMR experiments in this study.

The DNP-NMR system used in this study is primarily composed of a Bruker DNP-NMR AVANCE III 400 MHz (9.4 T) spectrometer connected through a corrugated transmission line to a gyrotron generate 263.7 GHz μwave radiation. The NMR measurements were performed with 3.2 mm HXY triple-resonance MAS probes. Commercially available Bruker MAS probes for solid-state NMR at room temperature and DNP-NMR at 100 K, and a homebuilt probe was

used for DNP-NMR at 30 K [56]. The DNP sample for PNCs was prepared by impregnation of the solid-state sample with the polarizing agent cAsymPol-TEK dispersed in the non-polar solvent tetrachloroethylene (TCE).

(E) NMR SEQUENCES OF INTEREST

Cross-Polarization (CP)

DNP allows for a large buildup of polarization on ^{1}H's, which have the highest gyromagnetic ratio out of all nuclei, while the gyromagnetic ratio of other commonly observed nuclei such as ^{13}C and ^{15}N is 4 times lower and 10 times lower respectively. This suggests that one way improve the sensitivity of NMR for nuclei with lower γ is to generate the polarization on a higher γ nucleus and transfer this polarization to the lower γ nucleus, especially when the polarization is initially built up on 1H's through DNP. This is achieved through the cross-polarization (CP) pulse sequence [58, 80, 81].

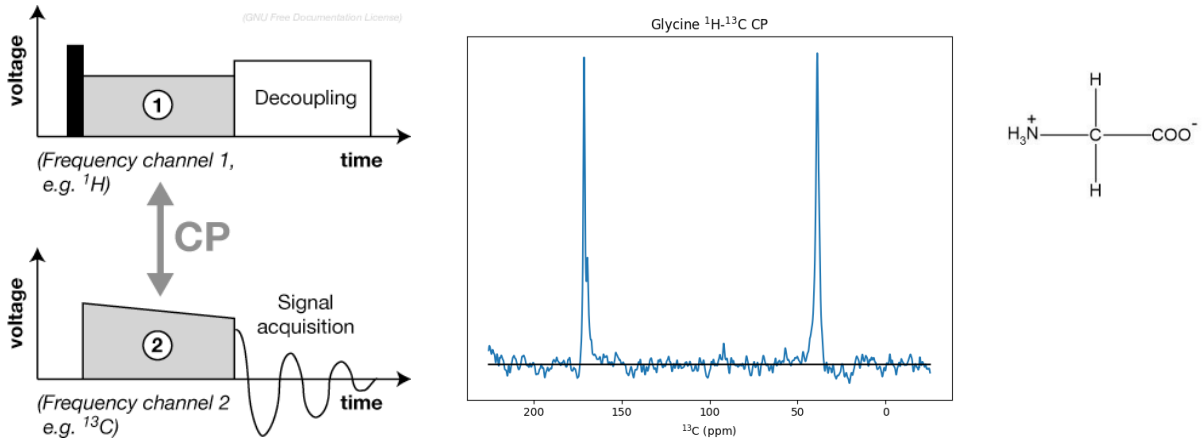

Figure 5: The CP pulse sequence (left), glycine ^{13}C CP spectrum (center), and structure of glycine (right)

The CP sequence (Figure 5) operates through heteronuclear dipolar coupling between the two nuclei, usually ^{1}H and X, which is a low γ nucleus. A coherence is initially generated for ^{1}H in the transverse plane, following which two in-phase spin-lock pulses are applied on the two nuclei. This allows mixing between the two nuclear spins through the dipolar coupling operating between them, resulting in the development of polarization on X, the magnitude of which is greater than that being developed upon direct saturation of X. The extent of mixing depends upon the strengths of the RF pulses on both channels, as well as the time for which the CP pulses are active. Under MAS conditions, optimal CP is achieved at Hartmann-Hahn sideband-matching conditions where the RF strengths ω_1^{H} and ω_1^{X} are related as follows:

Equation 5

$$\omega_1^{\mathrm{H}} - \omega_1^{\mathrm{X}} = \pm\omega_{\mathrm{R}}, \pm 2\omega_{\mathrm{R}}$$

where ω_{R} is the MAS rate.

The CP experiment for heteronuclei is usually set up on a reference compound before the real sample. ^{13}C and ^{15}N are standard heteronuclei for which CP conditions can be optimized using glycine (Figure 5). Unlabeled glycine powder at room temperature has been used an example to test ^{1}H→^{13}C CP efficiency at a MAS rate of 8000 Hz.

The ^{13}C CP spectrum is shown in Figure 5. Keeping the ^{1}H power level fixed, the ^{13}C power level was increased to find the position where the carbonyl (C') signal has the maximum intensity. There were 3 points found in this optimization scan (Figure 6) with a local maximum of intensity, corresponding to (1) $\omega_1^{\mathrm{H}} - \omega_1^{\mathrm{X}} = \omega_{\mathrm{R}}$, (2) $\omega_1^{\mathrm{H}} - \omega_1^{\mathrm{X}} = 0$, and (3) $\omega_1^{\mathrm{H}} - \omega_1^{\mathrm{X}} = -\omega_{\mathrm{R}}$. (2) is the static Hartmann-Hahn matching condition, and the intensity of the C' signal at this condition decreases when the MAS rate is increased (Figure 6). This is because of the more efficient averaging of the dipolar coupling at higher spinning speeds.

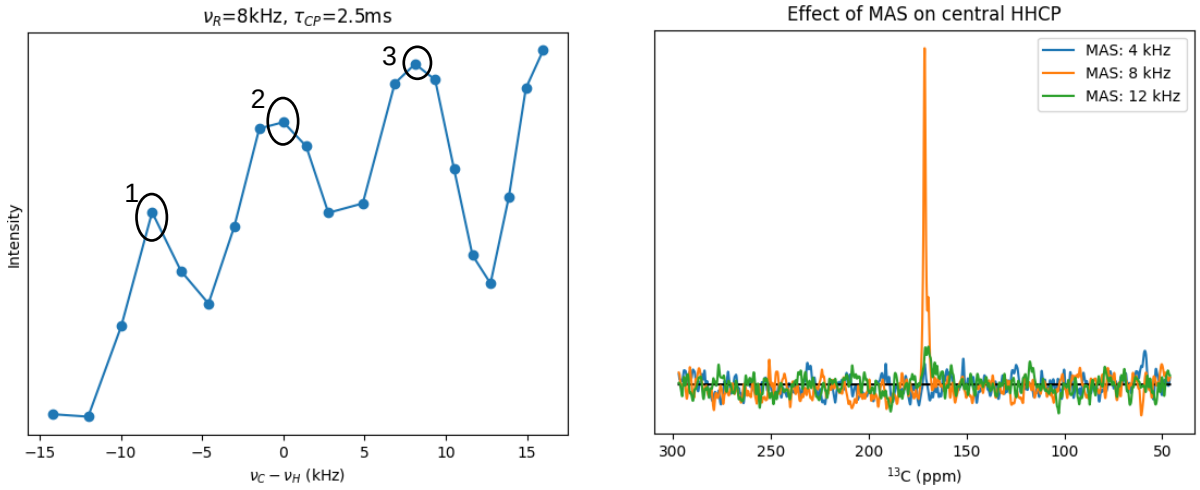

Figure 6: CP calibration - Demonstration of RF matching (left) and effect of MAS on static CP (right)

Glycine has two distinct C's which have different connectivities and distances to the ^{1}H's in the molecule. The strength of dipolar coupling depends on the distance between the heteronuclei I and S as follows:

Equation 6

$$d_{IS} = \hbar\left(\frac{\mu_0}{4\pi}\right)\frac{\gamma_I\gamma_S}{r_{IS}^3}$$

This results in different dipolar coupling constants and hence different CP buildup rates for the two C's, which is evident from the CP buildup curves (Figure 7). C_α builds up much faster than C' due to its proximity to the $^1H_\alpha$'s. However, the C_α peak decays at longer CP contact times due to faster T_2 relaxation. The differential buildup demonstrates that CP intensities of different peaks in the spectrum cannot be used for quantification, especially when there is an extensive homonuclear spin network for ^1H's in the sample.

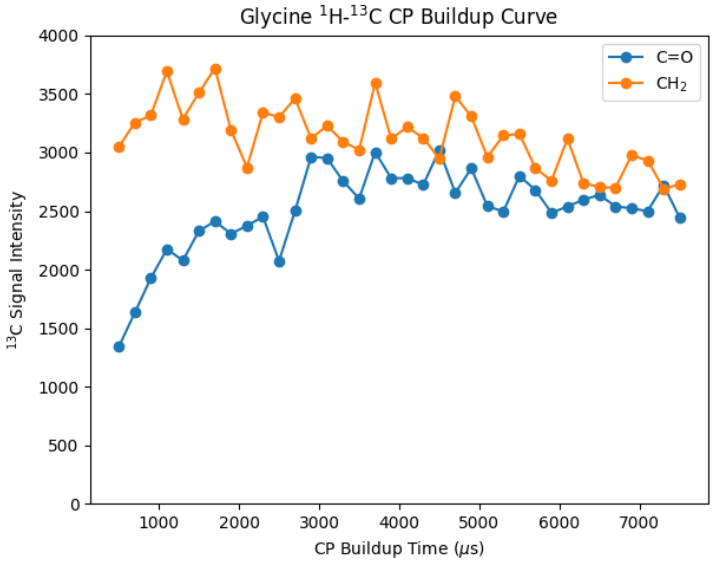

Figure 7: Glycine ^{13}C CP buildup curve

MAS results in averaging of the dipolar coupling, which negatively effects the CP transfer, even for sideband-matching conditions. CP efficiency can be improved by the use of variable amplitude contact pulses such as ramp CP [58], which is also less sensitive to deviations from the Hartmann-Hahn matching conditions.

2D Heteronuclear Chemical Shift Correlation (HETCOR)

CP involves the transfer of magnetization from ^1H to a heteronucleus X, such as ^{13}C and ^{15}N, through the heteronuclear dipolar coupling between them. This process suggests that CP can be used to directly observe the contacts (in terms of proximity) between ^1H's and the heteronuclei through the transfer of coherence at CP short contact times, which is the principle of two-dimensional heteronuclear chemical shift correlation (HETCOR).

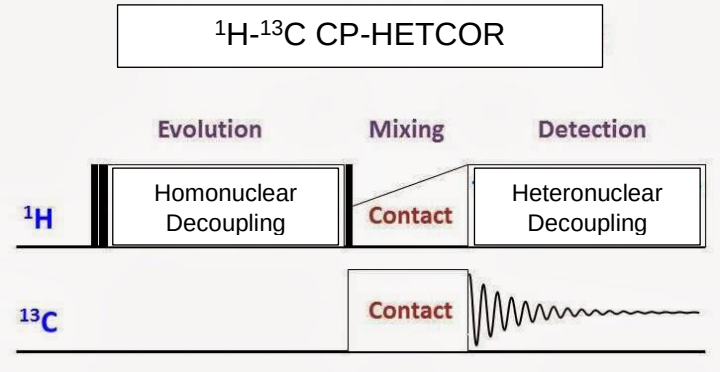

Figure 8: CP-HETCOR Pulse Sequence

Two-dimensional NMR experiments involve the following four steps: (i) a preparation period, where an initial coherence is created by the application of appropriate RF pulses, (ii) an evolution period for the initial coherence which usually corresponds to one of the nuclei, (iii) a mixing period, where the coherence is modified by the application of RF pulses to a state that can be detected, and (iv) a detection period, where the FID of this new coherence is recorded, which usually corresponds to the other nucleus in the spin pair. In CP-HETCOR (Figure 8), the initial coherence is prepared on ^{1}H's, which is allowed to precess in the evolution period. The mixing period here is the CP transfer from ^{1}H's to X, followed by detection of the X coherence evolution. The evolution period is incremented after the collection of each FID in a series of successive experiments to produce a two-dimensional time domain dataset which is processed into a two-dimensional frequency spectrum. This spectrum for CP-HETCOR is composed of peaks at the positions corresponding to ^{1}H's in the indirect dimension and X in the direct dimension. The CP-HETCOR peaks correspond to contacts between ^{1}H-X pairs. The peak intensities can be compared to provide an idea of the proximity between the heteronuclear spin pairs, as intense peaks suggest shorter internuclear distances and vice-versa.

The heteronuclear connectivities can be discerned from a CP-HETCOR spectrum effectively only if the peaks are resolved, which becomes increasingly difficult for broader spectra. As explained in section (B), spectral broadening in the solid-state arises from the internal anisotropic interactions, the effect of which is not completely removed by MAS. Thus, decoupling RF pulses need to be used. In the direct dimension, especially for heteronuclei with lower abundance, the primary interaction is the ^{1}H-X dipolar coupling. Heteronuclear decoupling sequences are used during the detection period, where pulses are continuously applied on ^{1}H while the FID for X is recorded. Heteronuclear decoupling during detection is standard and used in all the solid-state NMR experiments mentioned here. Broadening in the indirect dimension is more difficult to deal with, as it arises from homonuclear dipolar coupling

between ^{1}H's which are highly abundant, and the homonuclear dipolar coupling between them is very strong and extends through a large network. This necessitates the need for homonuclear decoupling during the evolution period, which are cycles of RF pulses applied on ^{1}H [82]. By the use of analytical techniques such as average Hamiltonian theory [58], it has been determined that the removal of the homonuclear dipolar interaction is accompanied by a modulation of the evolution due to chemical shift. Essentially, the chemical shifts are scaled by a factor that is specific to homonuclear decoupling sequence being used [62].

Assignment of the CP-HETCOR spectrum that uses homonuclear decoupling during detection requires the accurate determination of the chemical shift scaling factor in the indirect dimension. This has been done by setting up CP-HETCOR on the reference compound histidine at 8 kHz MAS with a 1 ms contact pulse.

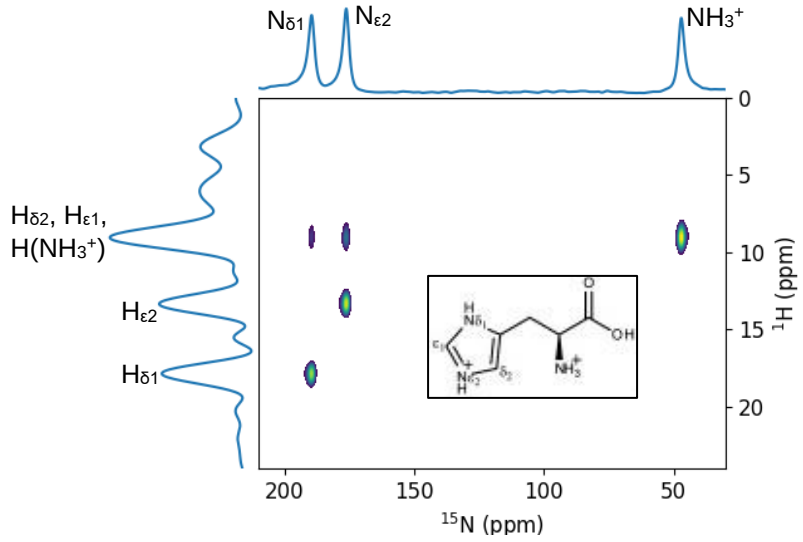

Figure 9: ^{1}H-^{15}N CP-HETCOR spectrum of histidine (structure in inset)

The ^{1}H-^{15}N CP-HETCOR spectrum is shown in Figure 9. The windowed LG4 homonuclear decoupling sequence [62] was used during t_1 evolution, as it not very sensitive to RF inhomogeneities. This is used for all subsequent CP-HETCOR experiments shown in this study. Spectral assignment was done using [71], from which the chemical shift scaling factor in the indirect dimension for this homonuclear decoupling sequence was calculated to be 0.34 which is in agreement with the theoretically calculated value [62].

Rotational-Echo Double Resonance (REDOR)

As mentioned previously in equation 6, the distance r between two nuclei is encoded into the dipolar coupling constant d_{IS} between them. The heteronuclear dipolar coupling Hamiltonian is given below:

Equation 7

$$\hat{H}_{dd} = -d_{IS}\, P_2(\cos\beta)\, 2\hat{I}_z\hat{S}_z$$

where β is the angle between the I-S internuclear vector and the external magnetic field, and $P_2(cos\beta) = (3\cos^2\beta - 1)/2$.

The dipolar coupling Hamiltonian, being anisotropic, is averaged under MAS due to modulation of the spatial part $P_2(\cos\beta)$, which can be understood as the periodic modulation of the local dipolar field on spin I. This averaging effect of the field of spin S on spin I is periodic, repeating after every rotor period. Thus, the averaging can be interrupted by inverting the sign of this local field using a π pulse on spin S in the middle of a rotor period (Figure 10). This results in the reintroduction of dipolar coupling by modulation of the spin part of the Hamiltonian, which is observed through a reduction in the intensity of the I spin signal. This dephasing effect is the principle on which rotational-echo double resonance (REDOR) operates [63]. Experimentally, the observed reduction of the I spin signal intensity S includes dissipative effects from T_2' relaxation during the REDOR blocks. T_2' relaxation is isolated by another experiment where no π pulses are applied on the S spin and the signal S_0 is recorded. The ratio S/S_0 isolates the effect of reintroduction of the dipolar coupling. The extent of dephasing of the signal S is dependent on for how long the dipolar coupling is reintroduced, which is essentially the number of rotor periods where the intermediary π pulses on spin S are applied. The experiments S and S_0 are repeated for an increasing number of rotor periods (also known as the mixing time τ_{mix}). The curve for S/S_0 vs τ_{mix} is analyzed to extract the dipolar coupling constant and hence internuclear distance, an important structural and geometrical property of any system.

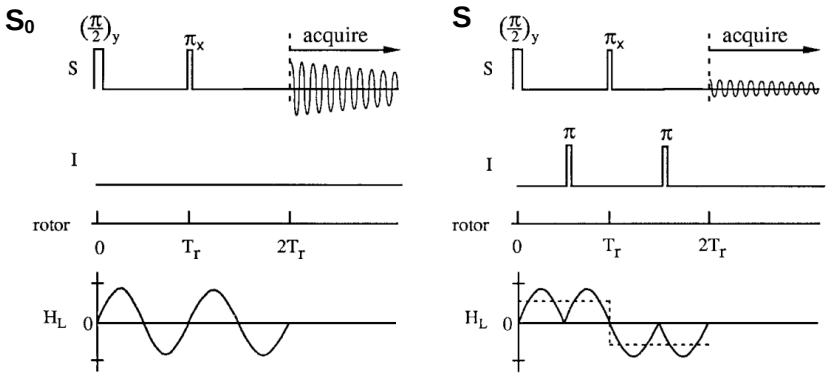

Figure 10: The REDOR pulse sequence, depicting the dipolar coupling averaging under MAS (left) and reintroduction (right)

The REDOR experiment for dephasing of ^{13}C by ^{15}N was tested in DNP conditions (30 K) on the uniformly labelled tripeptide MLF (methionine-leucine-phenylalanine) at a MAS rate of

7.5 kHz. The DNP sample for MLF was used from [56], with the polarizing agent cAsymPol-POK. RF pulses of 36 kHz and 25 kHz were used for the ^{15}N and ^{13}C π pulses respectively. The DNP enhancement for ^{15}N was 32, evaluated from the ratio of the triplet signal intensity in microwave on and off conditions (Figure 11).

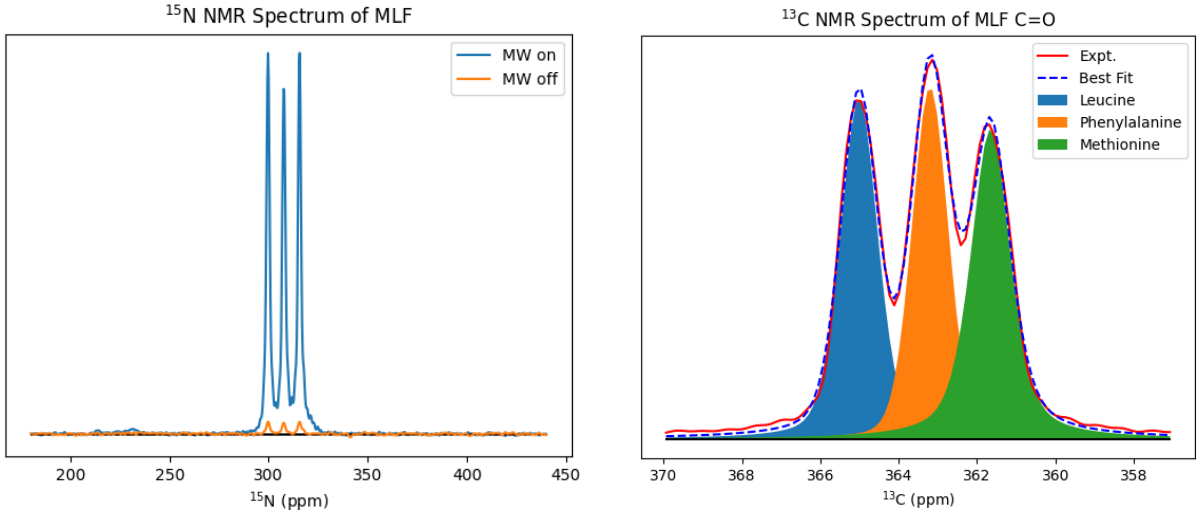

Figure 11: DNP-enhanced MLF spectra: ^{15}N (Left) and ^{13}C (Right). The ^{15}N spectrum shows a DNP enhancement of 32.

The ^{13}C NMR spectrum for the carboxylate (C') region (Figure 11) was assigned according to [64] and the corresponding C' intensities of each amino acid were calculated. The REDOR dephasing curve $S/S_0(\tau_{mix})$ (Figure 12) was analyzed by the lmfit() module in Python. The fitting function was constructed by incorporating REDOR simulations in SIMPSON through a shell script that could take the fitting parameters (which are the internuclear C'-N distances) as input. Best-fit parameters have been tabulated in Table 1. There is a good agreement with the PDB crystal structure 1Q7O. The experimental parameters such as pulse lengths and pulse powers for ^{13}C and ^{15}N were taken from this experiment and applied to the perovskite sample.

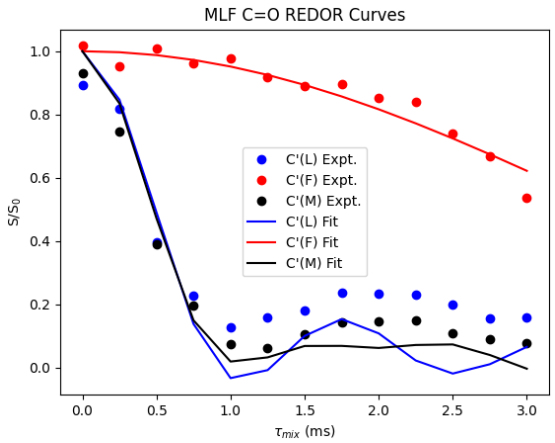

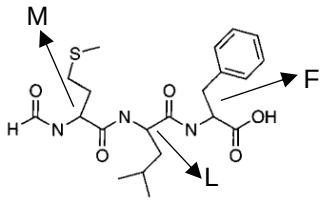

Figure 12: REDOR dephasing curve (left) for MLF (structure at right, with amino acid assignment)

Table 1: REDOR distances between carboxylates (C') and nitrogens (N) of MLF amino acids

	C'_M	C'_L	C'_F
N_M	2.5 ± 0.3 Å	5.6 ± 0.7 Å	7.1 ± 1.8 Å
N_L	1.3 ± 0.1 Å	2.4 ± 0.2 Å	4.8 ± 0.4 Å
N_F	3.6 ± 0.2 Å	1.3 ± 0.1 Å	2.5 ± 0.5 Å

Transferred-Echo Double Resonance (TEDOR)

As discussed previously, CP-HETCOR enables the observation of contacts between ^{1}H and heteronuclei X through the dipolar coupling between them. Similarly, the concept of manipulating the coherence on the nucleus I by the application of π pulses on the nucleus S can be extended to construct a NMR experiment that displays the dipolar connectivities between I-S spin pairs in a two-dimensional spectrum. This experiment is known as transferred-echo double resonance (TEDOR) [65].

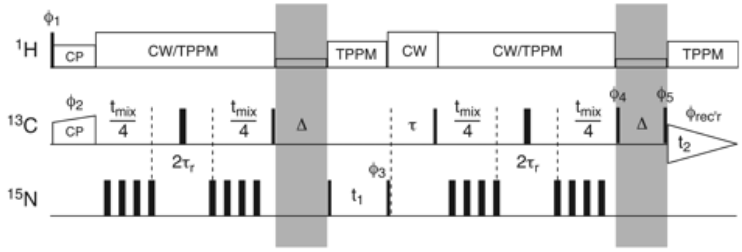

Figure 13: The zf-TEDOR pulse sequence

TEDOR (sequence in Figure 13) is composed of a preparation period where the transverse magnetization on I is introduced by CP from ^{1}H's, followed by a set of REDOR blocks where the I-S dipolar coupling is reintroduced, which is used to prepare a coherence on the S spin by the application of RF pulses. This S spin coherence is allowed to evolve which is used to frequency-label the in the indirect dimension (similar to the evolution period for ^{1}H in CP-HETCOR). The subsequent mixing period involves the application of RF pulses followed by another set of REDOR blocks that creates observable I spin coherence through reintroduction of the I-S dipolar coupling. The FID of this I spin magnetization is recorded. This experiment, when done for a single REDOR mixing time, i.e., a single fixed number of REDOR blocks, generates a 2D time domain dataset similar to CP-HETCOR which is processed to produce a 2D frequency spectrum that shows peaks for the dipolar-connected I-S pairs. The same experiment can be recorded with for a series of REDOR mixing times, and the I-S peak

intensities can be extracted as a function of τ_{mix}, analysis of which reveals the internuclear distances between each of the I-S pairs visible on the 2D spectrum.

The TEDOR experiment has multiple advantages over the aforementioned REDOR experiment. Firstly, TEDOR allows direct visualization of the dipolar-coupled I-S pairs through the two-dimensional spectrum. Secondly, the signal on the detected nucleus I is obtained with a direct transfer to and from the other nucleus S instead of an indirect dephasing effect, especially for low dipolar coupling. This ensures that the dipolar coupling being studied is with the intended S nucleus and not with some other nucleus with a broad lineshape that resonates at a frequency close to S (such as ^{35}Cl when the intended S nucleus is ^{15}N).

The TEDOR peak intensities have a different mixing time profile than REDOR. The coherences on each of I and S are created by transfer of magnetization from the other nucleus through the reintroduction of the I-S dipolar coupling during the REDOR blocks. Thus, instead of decay of the signal as in REDOR, there is a buildup of the signal in TEDOR as the dipolar coupling is introduced for longer and longer mixing times. This buildup is accompanied with a T_2' relaxation, which cannot be isolated as it is not feasible to perform a reference experiment like S_0 in REDOR. Also, the magnitude to which the TEDOR signal builds up cannot be predetermined. Thus, analysis of the TEDOR experiment requires three parameters, namely the internuclear distance, the T_2' relaxation rate, and the absolute magnitude of the buildup. This approach has been applied to the study of ligands on $CsPbBr_3$ PNCs.

(F) DENSITY FUNCTIONAL THEORY (DFT)

The electronic structure of materials governs their electrical, optical, and magnetic properties, and many other attributes of physical relevance. However, it is not possible to obtain an exact solution to the Schrödinger equation for a many-body problem, as is the case for physical systems of interest. Density functional theory (DFT) provides a way to solve this problem, and can be used to study a variety of materials including PNCs.

As the name suggests, DFT operates on the principle that the total energy of any given system can be written as a functional of its electron density. Also, the properties of the system can be determined by the ground state electron density. These ideas are ingrained in the two Hohenberg-Kohn theorems [86]. The Schrödinger equation is solved by the Kohn-Sham approach, wherein the many-body problem is mapped to an auxiliary independent-electron problem experiencing an effective potential that is comprised of the original external potential, an inter-electronic repulsion component (known as the Hartree term), and an exchange-

correlation potential that bundles up the many-body interactions [87]. Solving this auxiliary system for bulk solids requires the use of the inherent periodicity of the lattice through the Bloch theorem to construct the extended wavefunctions, which can be written as the product of a wave-like part in real space and a periodic part which has the same periodicity as that of the lattice. The periodic part is expanded in a plane wave basis set in the reciprocal space using reciprocal lattice vectors. This basis set can be truncated by introducing a kinetic energy cutoff, since basis vectors with high kinetic energies have a lower contribution to the expansion of the total wavefunction. In order to account for the infinite number of electrons across the unit cells, theoretically an infinite number of k-points should be used for the wave like part. However, since the electronic wave functions at k-points very close together are almost identical, it is possible to represent the electronic wave functions over a region of k-space by the wave functions at a single k-point. Thus, a finite set of k-points in the first Brillouin zone can be used for the wave like part of the Bloch wavefunction.

The resulting Kohn-Sham equations are solved iteratively and self-consistently to yield the ground state electronic density of the system. As most chemical and physical properties of systems depend on the overlap of the wave functions of the valence electrons, the core electrons are not explicitly considered in these calculations to reduce the computational cost. The divergence of the ionic Coulomb potential at r=0 is overcome by using a pseudopotential. Also, the valence wave functions exhibit fast oscillations in the core region to satisfy orthonormality conditions, which would require an unyieldingly large plane wave basis set to replicate accurately. The true valence wave functions are smoothened out in the core region by using pseudo wave functions which reduces the basis set size. In summary, physico-chemical properties of materials, given their crystal structure, can be calculated *ab initio* by DFT using a plane wave basis set, along with an appropriate exchange-correlation functional and the pseudopotential approximation [66].

DFT calculations on surfaces, such as in this study, necessitate the exposure of the surface of choice by truncating the interaction with the next unit cell through the addition of a vacuum region. However, for asymmetric systems, the asymmetric electron densities of neighboring cells result in the development of a spurious dipole moment which can affect the calculated properties, even for large vacuums. This spurious dipole moment is eliminated through dipole correction [67], which entails the addition of a sawtooth potential that cancels out the electric field due to this spurious dipole potential. The edges of the sawtooth potential must lie in the vacuum region with no electron density to avoid problems in calculating relevant derivatives.

The computed electron density can be used to calculate shielding constants for the different nuclei in the system which determines their NMR chemical shifts. However, calculating how the electron density shields the nucleus necessitates the use of the true core behavior of the valence wavefunctions. The pseudopotential approximation results in the loss of information about the core electron density. This is why projector-augmented wave (PAW) pseudopotentials are used, which allow for the conversion and reconversion between pseudo- and all electron-wavefunctions through a linear transformation. The shielding constants are obtained by calculating the induced electronic magnetic field upon the application of an external magnetic field using perturbation theory. However, the ground state wavefunctions are not gauge-independent, which is why a gauge transformation is included in the PAW linear transformation. This method to calculate the shielding effects is known as the gauge-including projector-augmented wave method (GIPAW) [68].

All these methods are incorporated in modules in a wide variety of quantum chemical calculation software. In this study, the software of choice is Quantum Espresso, version 7.1 [69].

RESULTS AND DISCUSSION

(A) SOLID-STATE NMR AT ROOM TEMPERATURE

The solid-state powdered sample with the labelled ligands was packed into a 3.2 mm thick wall zirconia rotor and was spun at a MAS rate of 16 kHz. The ^{1}H NMR spectrum (Figure 14) was recorded at room temperature with a recycle delay of 7 s and 16 scans. This was a direct excitation spin-echo experiment, performed with 85 kHz RF field ^{1}H pulses. ^{1}H chemical shifts were referenced with respect to adamantane (1.82 ppm) as in [70]. The spectrum has three sections, namely the aliphatics from the ligand tails in the region 0 ppm to 2.5 ppm, the olefinic region from oleic acid around 5.0 ppm, and signals in the 7.0 ppm to 7.5 ppm region. The latter region contains sharp signals from traces of solvents such as diphenyl ether, under which lies a broad signal from the ammonium ^{1}H's. The ^{1}H chemical shift assignment has been performed in accordance with [50].

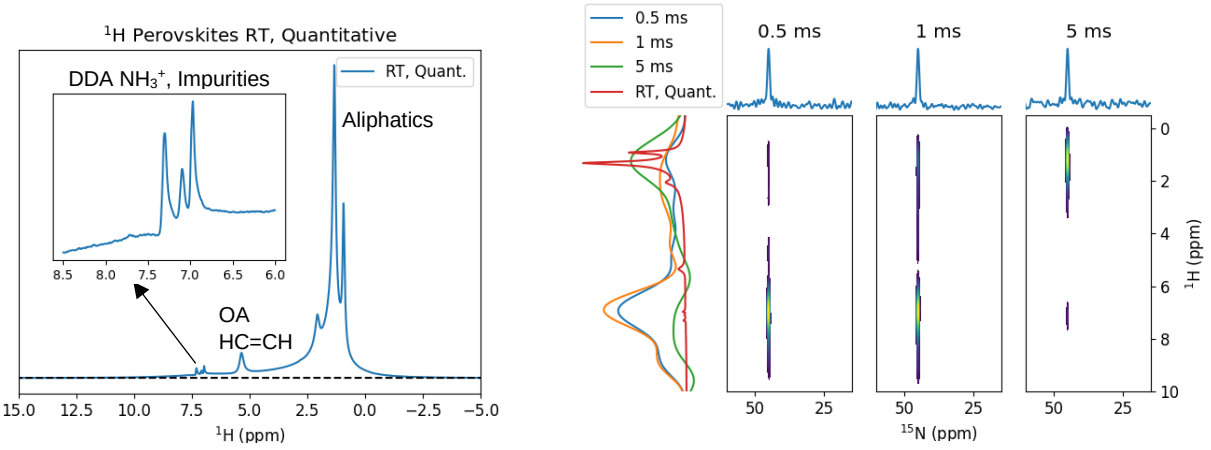

Figure 14: Solid-state spectra at room temperature: 1D ^{1}H (left) and ^{1}H-^{15}N CP-HETCOR at variable CP contact times (right)

The assignment of the ammonium signals was confirmed by ^{1}H-^{15}N CP-HETCOR (Figure 14) at room temperature, at a MAS rate of 8 kHz. A recycle delay of 2 s was used, along with 64 scans in the direct dimension and 64 points in the indirect dimension. The CP matching conditions for the contact pulses were taken from a previous reference experiment with histidine, which was also used to reference the ^{1}H and ^{15}N chemical shifts [71]. The SWf-TPPM heteronuclear decoupling sequence was used during acquisition [83]. A Lee-Goldburg cycle (LG4) was used for homonuclear decoupling of the ^{1}H's. The previous histidine experiment was used to calculate the scaling factor for the ^{1}H chemical shifts, which is 0.34. Three different CP contact times, namely 0.5 ms, 1 ms, and 5 ms were used to determine the spatial proximity between the observed species in the CP-HETCOR spectrum. The ^{15}N peak

correlated with two ^{1}H peaks, one of which corresponded to the aliphatic region as determined from the one-dimensional ^{1}H spectrum. The other peak at 7.0 ppm showed a greater intensity at lower contact times, especially 0.5 ms. This suggests that this peak corresponds to a ^{1}H species which is in closer proximity to the ^{15}N in the amine functional group compared to the aliphatics. Also, the number of ^{1}H's for this moiety must be lesser than the aliphatics as its relative intensity decreases when CP contact time is increased and aliphatic ^{1}H's further away can correlate with the functional group. These observations lead to the conclusion that the ^{1}H peak at 7.0 ppm corresponds to the ammonium ^{1}H's. Thus, the ^{1}H NMR spectrum complemented by ^{1}H-^{15}N CP-HETCOR shows that both oleic acid and dodecylamine are present in the sample and responsible for surface stabilization of the PNCs. Also, the appearance of the ammonium peak at 7.0 ppm indicates that dodecylamine binds to the surface of the PNCs in the protonated state, otherwise the signal would have appeared around 0.5 ppm.

A quantitative room temperature spectrum of ^{13}C was recorded, at a MAS rate of 8 kHz. The TPPM heteronuclear decoupling sequence was used during acquisition with 2048 scans. For the excited spins to reach thermodynamic equilibrium, the recycle delay is set to five times the relaxation time T_1 in quantification experiments. T_1 was calculated from a set of one-dimensional ^{13}C experiments with variable delay times. The spectral intensities were calculated as a function of the delay time by integrating under the ^{13}C peak(s) of choice, and fit to the equation:

Equation 8

$$S(t) = S_0\left(1 - e^{-\frac{t}{T_1}}\right)$$

This is a solution to the Bloch equations with one characteristic relaxation rate. The calculated T_1 is 6 s. The recycle delay for the quantitative ^{13}C experiment has hence been set to 30 s.

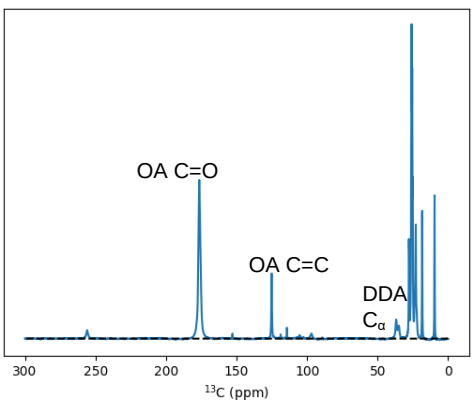

Figure 15: Quantitative solid-state room temperature ^{13}C spectrum

Chemical shift referencing of the ^{13}C spectrum (Figure 15) was performed with respect to adamantane [72]. The intense peaks in the region 0 ppm to 30 ppm can be attributed to the ligand backbone aliphatics [84]. The peak at 40 ppm belongs to the carbon in the alpha position relative to the functional group in dodecylamine. This can be confirmed from the TEDOR buildup curve analysis, as will be discussed in section (C). The peak around 125 ppm is assigned to the olefinic carbons of oleic acid with the help of $^{1}H \rightarrow ^{13}C$ CP-HETCOR as described later in this section. Finally, the intense peak at 180 ppm comes from the carboxylic carbon of oleic acid. This peak has a very high intensity even though it is from a single carbon because the of the selective labelling of the oleic acid at the functional group. The extent of labelling has been inferred from the intensities of the two characteristic oleic acid peaks. The natural abundance of ^{13}C is 1.1%, which is the entire contribution to the two carbons of the olefinic signal at 125 ppm. The contribution to the carbonyl peak at 180 ppm comes from both labelling and natural abundance of the unlabeled part. These relative intensities can be equated with the NMR peak intensities:

Equation 9

$$\frac{S_{C=O}}{S_{C=C}} = \frac{l + 1.1\% \times (100 - l)}{2 \times 1.1} \Rightarrow l = \frac{2.2}{0.989} \times \left(\frac{S_{C=O}}{S_{C=C}} - 0.5\right)$$

where l is the percentage of labelling, $S_{C=O}$ and $S_{C=C}$ are the integrated intensities of the carboxylate and olefinic peaks respectively. This gives a selective ^{13}C labelling on the carboxylic carbon of oleic acid by an amount of 15.74%, which is in accordance with the initial labelling of 15% used during synthesis.

The amount of labelling once quantified has been used to calculate the ligand ratio, i.e., the ratio between the number of oleic acid and dodecylamine molecules interacting with the PNCs. The dodecylamine is quantified using the C_α peak at 40 ppm, the entire contribution of which comes from the 1.1% natural abundance of ^{13}C as the alpha carbon is not labelled. On the other hand, the oleic acid is quantified using the carboxylic peak at 176 ppm for which the quantification method has been described in the previous paragraph.

Equation 10

$$\frac{S_{C_\alpha}}{S_{C=C}} = \frac{[DDA] \times 1.1}{[OA] \times (l + 1.1\% \times (100 - l))} \Rightarrow \frac{[OA]}{[DDA]} = \frac{1.1 \times S_{C=O}}{(l + 1.1\% \times (100 - l)) \times S_{C_\alpha}}$$

The oleic acid-to-dodecylamine ratio comes out to be 1:2.2. The fact that the surface passivation mechanism involves an excess of amines when compared to the acid is in

accordance with previous studies [50] which have reported an amine-acid ratio of 1:1.7 through solution NMR. The referenced study used solution-state NMR for quantification. The difference in the ligand ratios is presumably due to the drying protocol for solid-state sample preparation affecting the ligand equilibrium at the surface.

A ^{1}H-^{13}C CP-HETCOR spectrum was recorded at room temperature, at a MAS rate of 8 kHz. A recycle delay of 2 s was used, along with 128 scans in the direct dimension and 64 points in the indirect dimension. The CP matching conditions for the contact pulses were taken from a previous reference experiment with glycine. The heteronuclear decoupling sequence TPPM was used during acquisition. The Lee-Goldburg cycle (LG4) was used for homonuclear decoupling of the ^{1}H's. The previous histidine experiment was used to shift and scale the ^{1}H chemical shifts. Three different CP contact times as before were used. All the characterized ^{13}C peaks show up in the HETCOR spectrum (Figure 16) with 5 ms contact time. The same applies for the ^{1}H dimension, where peaks for the aliphatics, oleic acid vinylic ^{1}H's, and dodecylamine ammonium ^{1}H's show up.

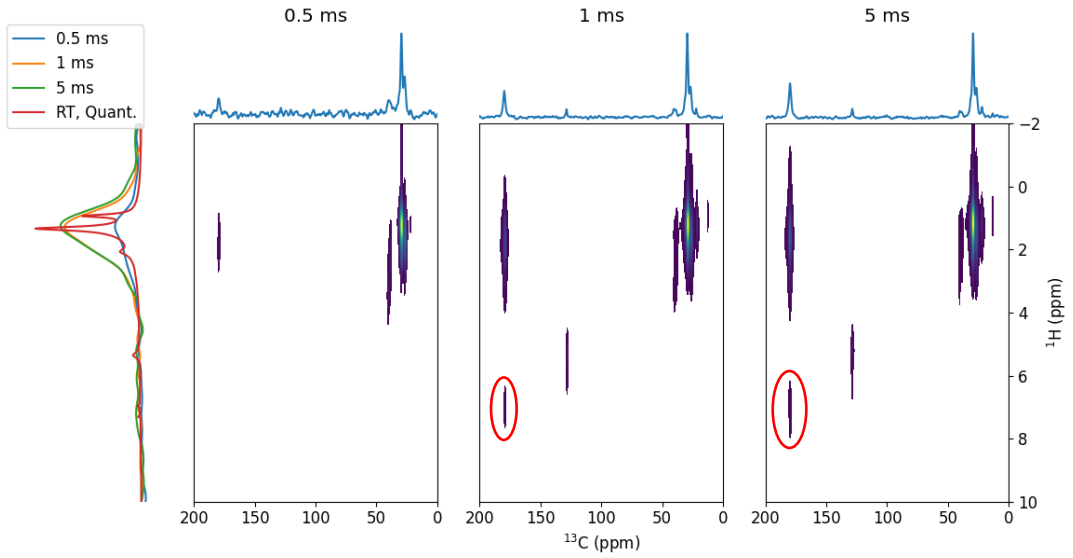

Figure 16: The ^{1}H-^{13}C CP-HETCOR spectrum. Correlation between oleic acid C' and dodecylamine NH_3^+ is circled in red.

For 0.5 ms contact time, correlation is seen only with the aliphatic ^{1}H's due to their large population. At 1 ms and 5 ms contact times, we see two new correlations appear. One of these is the expected correlation of the vinylic carbons of oleic acid to their own ^{1}H's. The new correlation is of greater interest, as it is representative of contacts between the carboxylic carbon of oleic acid and ammonium ^{1}H's of dodecylamine. This is evident of proximity between the amine and acid ligands, suggesting a ligand pairing mechanism at the PNC surface.

The interaction between oleic acid and dodecylamine has been further probed by TEDOR experiments as will be discussed in section (C).

(B) DNP-ENHANCED NMR AT 100 K

DNP experiments were performed at 100 K in a 3.2 mm thick-wall zirconia rotor. ^{1}H-^{15}N CP-HETCOR was performed at a MAS rate of 12 kHz. A recycle delay of 2.6 s was used, along with 16 scans in the direct dimension and 48 points in the indirect dimension. The CP matching conditions for the contact pulses were taken from a previous reference experiment with histidine, which was also used to reference the ^{1}H and ^{15}N chemical shifts. The TPPM heteronuclear decoupling sequence was used during acquisition with RF pulse strengths. The Lee-Goldburg cycle (LG4) was used for homonuclear decoupling of the ^{1}H's. The previous histidine experiment was also used to calculate the scaling factor for the ^{1}H chemical shifts, which is 0.34. Again, three different CP contact times were used.

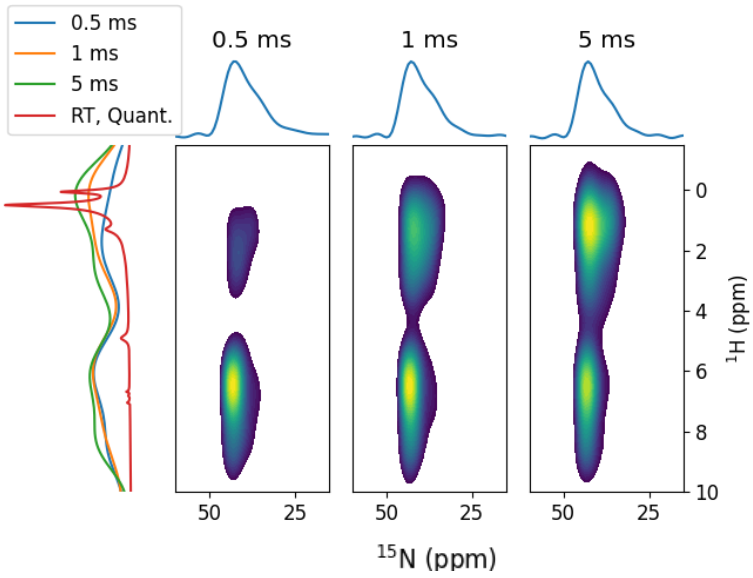

Figure 17:DNP-enhanced ^{1}H-^{15}N CP-HETCOR spectrum at 100 K, showing the broad ^{15}N peaks

The ^{1}H dimension shows the same peaks as in room temperature (spectrum in Figure 17). However, the ^{15}N spectral profile is much broader, and shows the presence of two distinct dodecylamine species, one corresponding to the main ^{15}N peak at 44 ppm, the other corresponding to a shoulder at 39 ppm. This difference between the 100 K and room-temperature ^{15}N peaks can be explained by the slowing down of the ligand dynamics at lower temperature that causes reduction in motional averaging. However, this difference could also arise due to perturbation of the equilibrium governing colloidal stabilization of the PNCs when the colloidal suspension is dried to produce the solid-state sample, especially if there is a ligand shell around the PNCs that can be disturbed due to drying.

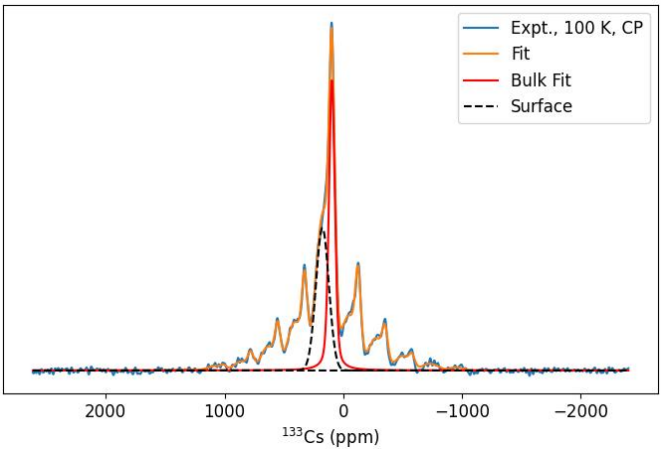

Figure 18: DNP-enhanced ^{133}Cs CP spectrum at 100 K, showing spinning sidebands and the two kinds of Cs species

The PNC surface was probed by a ^{1}H-^{133}Cs CP experiment, performed at a MAS rate of 12 kHz, with a recycle delay of 2.6 s and 64 scans. The CP matching conditions were optimized on this sample itself. The TPPM heteronuclear decoupling sequence was used during acquisition. CP contact time of 5 ms was used. In the ^{133}Cs spectrum (Figure 18), spinning sidebands can be observed due to the quadrupolar coupling which has been previously estimated to be 0.2 MHz for $CsPbBr_3$ [73]. The spinning sidebands are separated at the MAS rate, as expected. This sideband pattern was fitted to reveal two primary ^{133}Cs species. The first spectral component is a sharp peak around 100 ppm which has been assigned to bulk Cs. The other component is a broad peak in the 200 ppm region which has been assigned to surface Cs atoms [73]. The increased breadth of the "surface" signal has been studied in [73] and has been attributed to a combination of distinct peaks from Cs species 0.8 – 2.3 nm deep from the NC surface, as the ^{133}Cs chemical shift is very sensitive to its environment.

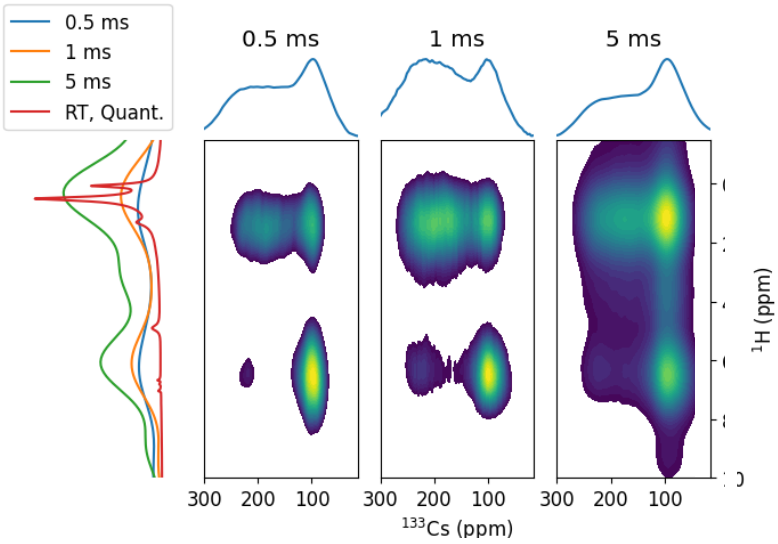

Figure 19: DNP-enhanced ^{1}H-^{133}Cs CP-HETCOR spectrum at 100 K

Ligand interaction with the PNC surface has been studied by ^{1}H-^{133}Cs CP-HETCOR experiments (spectrum in Figure 19). The same experimental parameters as in the ^{1}H-^{15}N CP-HETCOR experiment were used here, except for acquisition with 128 scans. The low contact time experiments, despite having lower intensity, show the more interesting immediate contacts between the heteronuclear pairs, as homonuclear ^{1}H coupling at higher contact times creates correlations with the entire ^{1}H spin network. ^{133}Cs HETCOR at low contact times is possible only because of DNP enhancement. As in the ^{1}H-^{15}N CP-HETCOR experiment, the indirect dimension shows peaks from the aliphatic and ammonium ^{1}H's. Correlation of ^{133}Cs with the ammonium ^{1}H's is clear evidence of the interaction of dodecylamine with the PNCs. The aliphatic signal can be from the ^{1}H's alpha to the functional group in both oleic acid and oleylamine. As the aliphatic signal shows up at CP contact times as low as 0.5 ms, it can be inferred that the ligands are in very close proximity to the surface, if not occupying surface vacancies. An interesting observation here is that the "bulk" ^{133}Cs signal shows a more intense correlation peak with the ammonium ^{1}H's compared to the "surface" signal. The solution to this apparent discrepancy lies in the fact that the sub-surface ^{133}Cs signal, i.e., the Cs atoms in the layer just below the topmost, appears at 95 ppm which is extremely close to the bulk chemical shift [73].

(C) DNP-ENHANCED NMR AT 30 K

Pseudo-3D TEDOR experiments were performed between ^{13}C and ^{15}N under DNP conditions at 30 K with the sample packed in a 3.2 mm thick-wall zirconia rotor, in order to investigate the interactions between the ligands. The experimental parameters were kept the same as the REDOR experiment for the tripeptide MLF which has been discusses previously. The ^{13}C and ^{15}N chemical shifts have been referenced with respect to MLF [64].

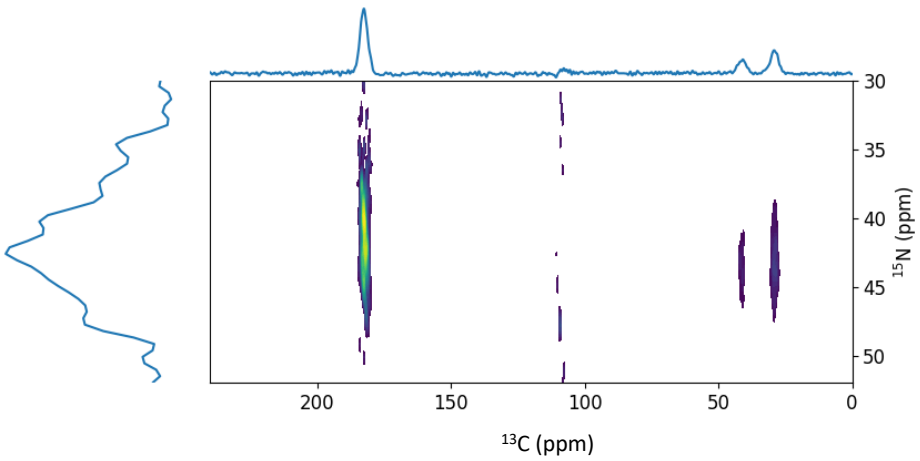

Figure 20: DNP-enhanced ^{15}N-^{13}C TEDOR spectrum at 30 K, obtained with a REDOR mixing time of 6.4 ms

The two-dimensional ^{15}N-^{13}C spectrum (Figure 20) obtained at a mixing time of 6.4 ms displays the contacts between the different ^{13}C and ^{15}N species. The broad ^{15}N peak composed of a main peak and a shoulder shows up in the indirect dimension. In the direct dimension, primarily three ^{13}C peaks are visible. The peaks at 36 ppm and 25 ppm fall in the aliphatic ^{13}C region (Figure 21). The evolution of these peaks with the increase in REDOR mixing time has been analyzed with spin dynamics simulations in SIMPSON combined with the lmfit() procedure in Python, where the fitting function can be described as follows:

Equation 11

$$S(\tau_{mix}) = A \times TEDOR(d_{IS}, \tau_{mix}) \times e^{-\tau_{mix}/T_2'}$$

where A is the magnitude of buildup, $TEDOR(d_{IS}, \tau_{mix})$ is the SIMPSON simulation with ^{13}C-^{15}N dipolar coupling d_{IS}, and T_2' is the transverse relaxation rate.

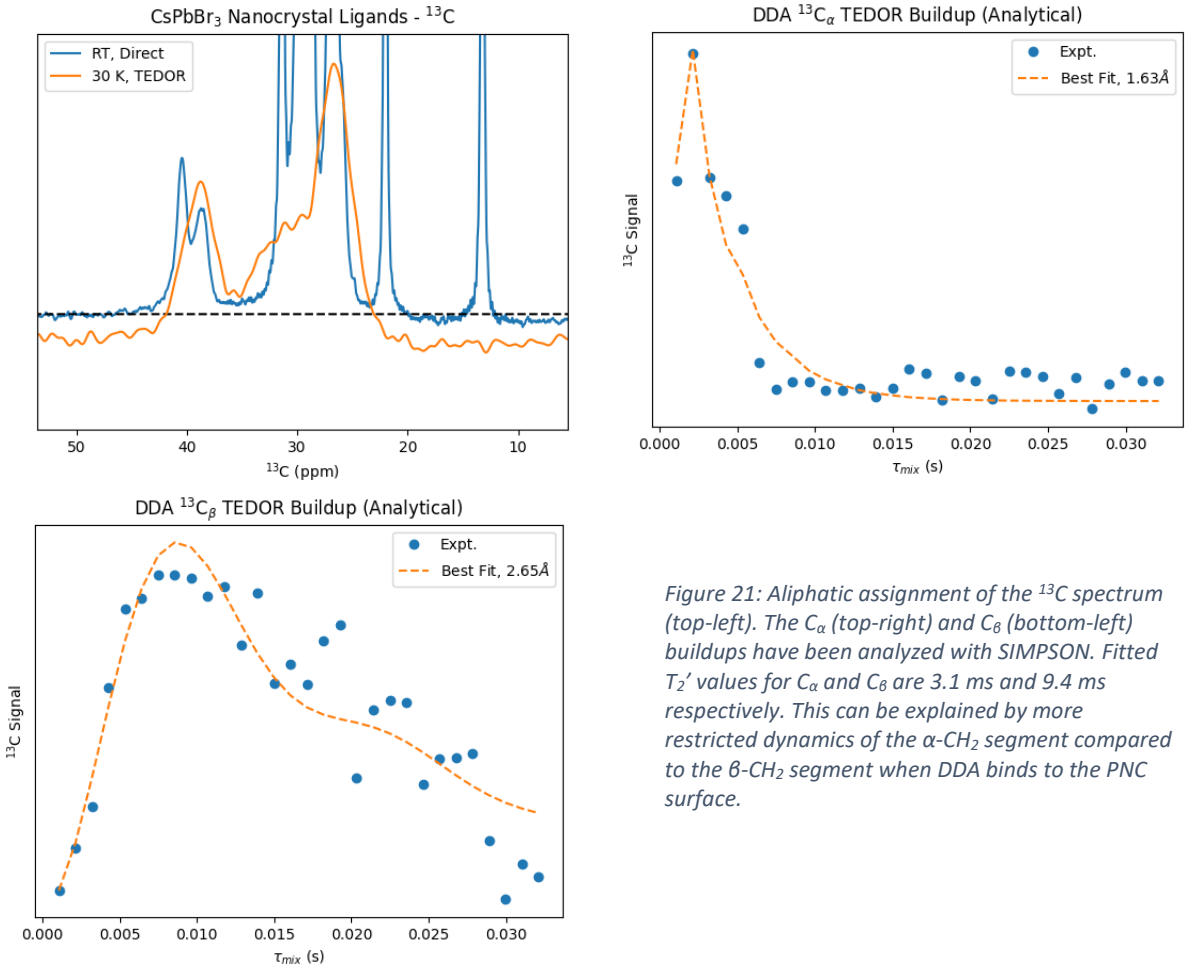

Figure 21: Aliphatic assignment of the ^{13}C spectrum (top-left). The C_α (top-right) and C_β (bottom-left) buildups have been analyzed with SIMPSON. Fitted T_2' values for C_α and C_β are 3.1 ms and 9.4 ms respectively. This can be explained by more restricted dynamics of the α-CH_2 segment compared to the β-CH_2 segment when DDA binds to the PNC surface.

Fitting the TEDOR buildup curve for the peak at 40 ppm shows a ^{13}C-^{15}N internuclear distance of 1.63 Å ± 0.4 Å (Figure 21). This peak can thus be assigned to the alpha carbon of dodecylamine, for which the ^{13}C-^{15}N internuclear distance in the crystal structure is 1.49

(PubChem CID 13583). Analysis of the buildup curve for the other peak at 27 ppm reveals a ^{13}C-^{15}N internuclear distance of 2.65 $\pm$ 0.5 Å (Figure 21). This peak can be attributed to the beta carbon of dodecylamine, for which the ^{13}C-^{15}N internuclear distance in the crystal structure is 2.47 Å. This TEDOR assignment for the alpha carbon of dodecylamine has been used for ligand quantification in section (A). The beta carbon is hidden under the large aliphatic ^{13}C peaks which have contributions from the entire carbon backbone from both dodecylamine and oleic acid.

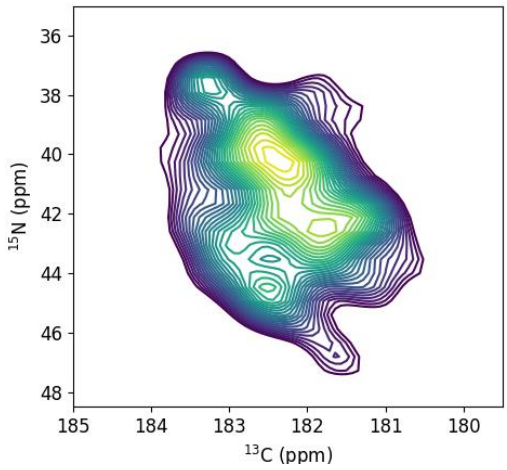

Figure 22: TEDOR cross-peak between oleic acid C' and dodecylamine N. The spectrum is composed of multiple features indicative of a variety of ligand pairs environments

The most intense correlation in the two-dimensional ^{15}N-^{13}C spectrum comes from the labelled carboxylic peak of oleic acid at 180 ppm (Figure 22). The appearance of this peak is a clear indication of the proximity between oleic acid and dodecylamine in the ligand passivation mechanism, as the internuclear distance must be less than 7 Å for the dipolar coupling to be sufficiently reintroduced. A variety of features are visible in this cross-peak, with at least four visible maxima. Also, the most intense correlation occurs with the ^{15}N shoulder at 40 ppm compared to the peak at 44 ppm, which was the main peak in the ^{1}H-^{15}N CP spectrum at 100 K. Thus, it can be inferred that the ^{15}N shoulder is indicative of dodecylamine molecules in proximity to oleic acid.

The buildup curve analysis for the carboxylic cross peak (Figure 23) is more involved due to the presence of multiple species in different environments as indicated by the spectral features. The carboxylic ^{13}C peak is deconvoluted into 5 components for each REDOR mixing time. The convolution is based upon the ^{13}C chemical shifts of the local maxima in the cross peak (185 ppm, 183.2 ppm, 182.5 ppm, 181.5 ppm, 180 ppm). The deconvolution (Figure 23) is

performed using the lmfit() module in python with a user-defined function to represent the peak profile that is composed of a superposition of Voigt lineshapes.

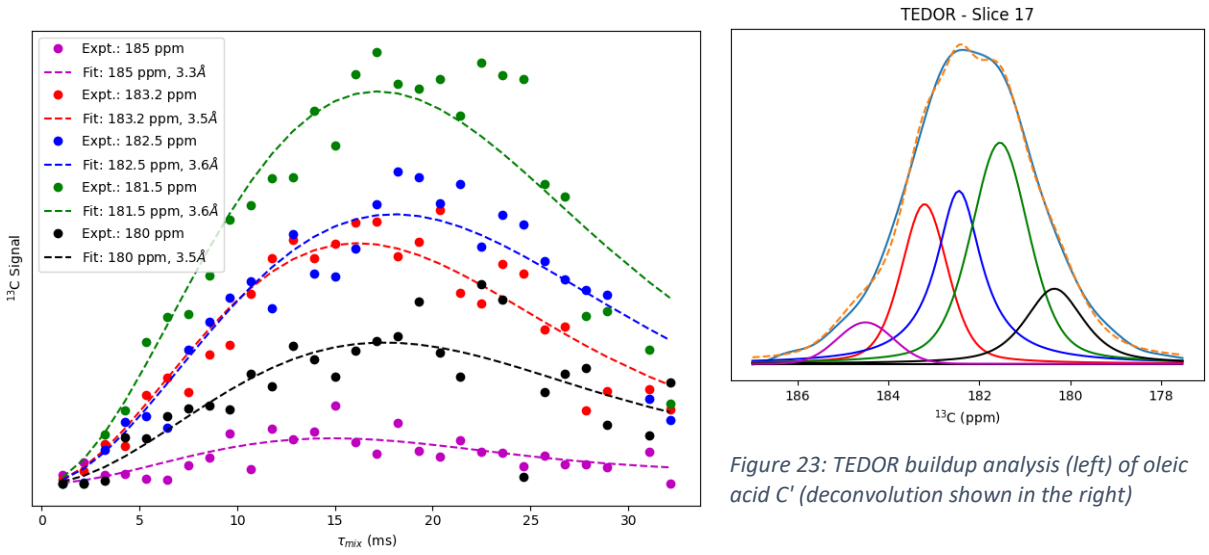

Figure 23: TEDOR buildup analysis (left) of oleic acid C' (deconvolution shown in the right)

The area under the deconvoluted peaks is evaluated to produce TEDOR buildup datasets for each of the ^{13}C chemical shifts in the carboxylic cross-peak. The individual datasets can be fit independently in each case with a single internuclear distance using the previously mentioned TEDOR buildup function in formula 11. This is because the probability of getting ^{15}N-^{13}C-^{15}N spin systems in proximity and other such spin networks is extremely low (< 0.4%) even after labelling. The peaks at 185 ppm and 180 ppm compete with the spectral noise due to their low intensity, which is evident from their buildup curves. The fitted data reveals a characteristic internuclear distance between the oleic acid carboxyl carbon and the dodecylamine nitrogen of 3.6 $\pm$ 0.8 Å. This is the first reported experimental evidence of ligand proximities and hence cooperative ligand binding on $CsPbBr_3$ PNCs. The experimentally obtained internuclear distance agrees very well with nearest neighbor Cs-Br distances in bulk $CsPbBr_3$, which are in the range of 3.75 Å to 3.8 Å, suggesting that a likely ligand binding mechanism is co-substitution of the functional groups of dodecylamine and oleic acid into surface Cs and Br vacancies respectively. Ligand binding to $CsPbBr_3$ surfaces has been studied by DFT calculations which is discussed in the next section

(D) DFT CALCULATIONS OF ENERGETICS

Computational Details

The DFT calculations were performed using the Quantum Espresso software, version 7.1. Ultrasoft pseudopotentials were used to describe the electron-ion interactions. The kinetic energy cutoffs used for wavefunction and charge density were set at 45 Ry and 450 Ry

respectively. Perdew, Burke and Ernzerhof parameterization of the generalized gradient approximation (GGA) was used for the electron-electron exchange and correlation. Integrations over the Brillouin zone were performed with 7×1×8 and 8×7×1 Monkhorst-Pack k-point meshes for (010) and (101) terminated slabs respectively. The calculations were sped up with the use of Marzari-Vanderbilt smearing of 0.007 Ry. Grimme-D2 dispersion correction was used to account for the Van der Waal's interactions. The parameters were used from [46].

Powder X-ray diffraction shows that the $CsPbBr_3$ PNCs crystallize in the orthorhombic *Pnma* structure. This is in agreement with the previous DFT study [46], which is why the $CsPbBr_3$ crystal structure from that study has been used here, with lattice parameters a = 7.561 Å, b = 8.529 Å, c = 11.891 Å. HRTEM images and their FFTs have shown that the PNCs are terminated by (010) and (101) planes. Phase contrast studies with defocusing in HRTEM have revealed the existence of both CsBr and $PbBr_2$ terminations. To simulate the surfaces, $CsPbBr_3$ slabs were built with (010) and (101) planes exposed, with the slab supercell composed of 1×1 surface unit cell. The (010) slabs were built from the primitive unit cell by simple translation of the atomic positions. The (101) slabs were constructed using the Atomic Simulation Environment (ASE) in combination with Python. Each of these slabs are composed of alternate charge-neutral layers of CsBr and $PbBr_2$, each of which were exposed vertically to simulate both kinds of surfaces. The surface exposure was simulated by adding a vacuum of 15 Å above the topmost surface of the slab.

The CH_3NH_2 energy was determined by relaxing the three-dimensional structure taken from PubChem CID 6329 in a cubic supercell of dimensions 40 bohr × 40 bohr × 40 bohr to simulate the molecule in the gas phase. The gas phase CH_3COOH energy was obtained by relaxing the three-dimensional structure taken from PubChem CID 176 in a cubic supercell of dimensions 40 bohr × 40 bohr × 40 bohr. Similarly, the energies of gas phase H_2 and Br_2 were obtained by relaxing the H_2 and Br_2 molecules with a standard bond length of 0.741 Å [88] and 2.281 Å (from the NIST chemistry webbook) respectively in their own cubic supercells of dimensions 40 bohr × 40 bohr × 40 bohr. The DFT-optimized bond lengths for H_2 and Br_2 in the gas phase were 0.752 Å and 2.314 Å respectively. The bulk CsBr energy was calculated using the stable structure mp-22906 from the Materials Project database. The three-dimensional structure for butylamine was taken from PubChem CID 8007, which was subjected to geometry optimization in the gas phase, in a cubic supercell of dimensions 40 bohr × 40 bohr × 40 bohr. Dipole correction was performed on the slab-ligand composites for ligand binding energy calculations.

Slab Thickness Convergence Tests

Surface atoms undergo relaxation to minimize the surface energy, adopting a configuration which is different from the bulk. The constructed slabs were hence relaxed to obtain the optimal configuration for the surface. The bottom two layers in the slabs were fixed during relaxation to emulate the bulk material in the core. An important parameter characterizing the applicability of a slab is its thickness. An optimal slab thickness is such that the constructed slab exhibits bulk-like properties within the slab after relaxation. The method to determine the optimal slab thickness involves testing the convergence in the value of the physical quantity under study as the number of layers in the slab is increased. The (010) plane-terminated slabs were already optimized in [46], with the slab thickness of choice being 10 layers. Optimization was performed on the (101) plane-terminated slabs.

The physical quantity of interest tested was the ligand binding energy, which is the subject of study for this section. The representative ligands used were the shorter methylamine (CH_3NH_2 or MA) instead of dodecylamine and acetic acid (CH_3COOH or AcOH) instead of oleic acid to reduce the computational cost. The binding mechanism used to test convergence for both CsBr- and $PbBr_2$-terminated slabs was the adsorption of methylammonium (abbreviated to MA), i.e., protonated methylamine, as it can be tested on both kinds of slabs. Calculation of the binding energy was done using the following reaction equation, in accordance with [46].

$$CH_3NH_2(g) + CsPbBr_3^{(surf)} + \frac{1}{2}H_2(g) \rightarrow CsPbBr_3^{(surf)} \cdots CH_3NH_3^+$$

For each of the CsBr- and $PbBr_2$-terminated (101) slabs, methylammonium was placed on a chosen tentative binding site, where the three ammonium ^1H's can interact through H-bonding with three surface Br atoms (structures in Figure 24). Relaxation calculations on this configuration were performed on the thinnest slabs to obtain a fixed adsorption site for methylammonium, after which more layers were added to the bottom of the slab and the relaxation calculations were repeated. The bottom two layers were fixed in all the slabs during relaxation to mimic the bulk material limit. Geometry optimization was performed in this manner as the adsorption site for each surface (CsBr or $PbBr_2$) should remain the same, with the only variable parameter being the number of layers in the slab.

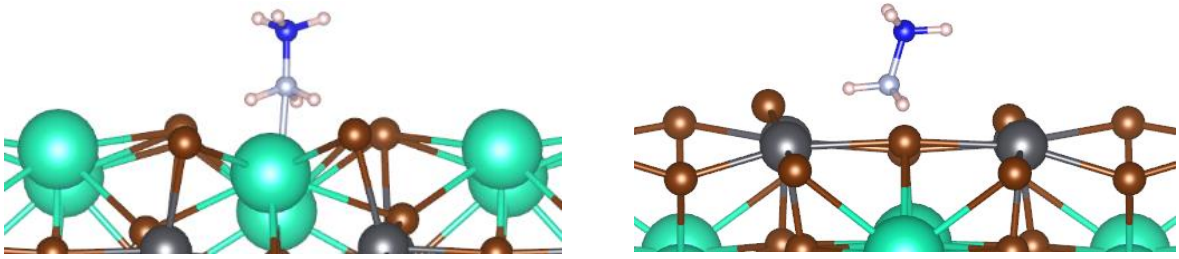

Figure 24: Adsorption configuration for slab thickness convergence test: CsBr termination (left) and $PbBr_2$ termination (right)

The binding energies for methylammonium adsorption for both CsBr and $PbBr_2$ (101) terminated slabs for variable slab thicknesses has been tabulated below in Table 2. For smoother convergence in case of CsBr-terminated slabs, dipole correction in the energies was performed. In both cases, the methylammonium binding energy converged for 6-layer thick slabs (change in binding energy < 0.01 eV). Thus, the optimal slab thickness for (101) slabs was determined to be 6 layers.

Table 2: (101) Slab Thickness Convergence Test

CsBr (101) Slabs			**$PbBr_2$ (101) Slabs**	
Slab Size	ΔE (eV)		Slab Size	ΔE (eV)
6 layers	0.38		4 layers	0.05
7 layers	0.39		6 layers	-0.12
8 layers	0.39		8 layers	-0.12

Ligand Length Tests

Once the slab thickness was optimized, the effect of shortening the ligand on the binding energies was tested. This was performed by replacing the methylammonium ligand with a longer butylammonium for the same binding mechanism. The calculations for the binding mechanisms with the butylammonium ligand were performed by replacing a methyl C-H bond from the optimized composite with methylammonium with the optimized butyl chain configuration, followed by adjusting the N-C-C-H dihedral angle to maintain the same molecular alignment as optimized butylamine. This was done to eliminate any extraneous effects from distortion of the butyl chain.

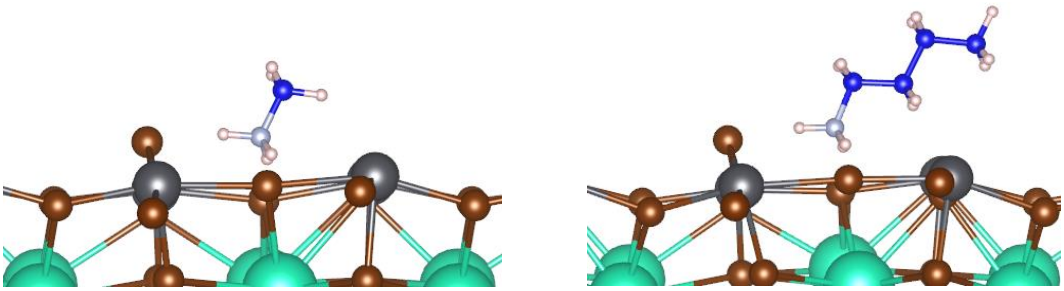

Figure 25: Ligand length tests for adsorption on the $PbBr_2$ surface: methylammonium (left) and butylammonium (right)

For the $PbBr_2$ termination, the binding mechanism tested was ammonium ligand adsorption (structure in Figure 25). The reaction equation is the same as the one used for slab thickness optimization:

$$RNH_2(g) + CsPbBr_3^{(surf)} + \frac{1}{2}H_2(g) \rightarrow CsPbBr_3^{(surf)} \cdots RNH_3^+$$

where R is CH_3- or $CH_3(CH_2)_3$-. The binding energy for methylammonium adsorption is -0.25 eV, while the binding energy for butylammonium adsorption is -0.36 eV. Ammonium adsorption operates through the formation of three H---Br hydrogen bonds, whose lengths are 2.196 Å, 2.224 Å and 2.240 Å for methylammonium adsorption. For butylammonium adsorption, the corresponding H---Br hydrogen bond lengths are 2.191 Å, 2.220 Å and 2.272 Å. This shows that the geometry of the ammonium group in the adsorption pocket does not change. Also, the orientation of the C-N bond with respect to the slab surface shows no appreciable variation (64.1º for methylammonium, 68.3º for butylammonium).

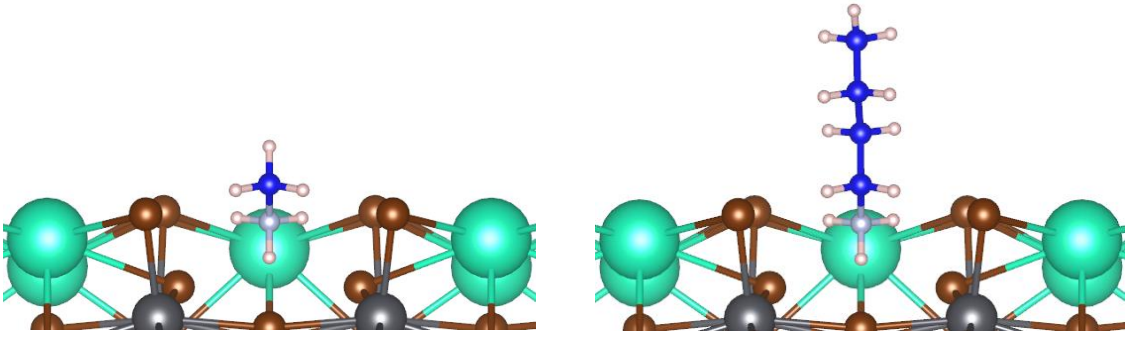

Figure 26: Ligand length tests for Cs substitution on the CsBr surface: methylammonium (left) and butylammonium (right)

For the CsBr termination, the binding mechanism tested was ammonium ligand substitution in the Cs vacancy (structures in Figure 26). The relevant reaction equation is given below:

$$RNH_2(g) + CsPbBr_3^{(surf)} + \frac{1}{2}H_2(g) + \frac{1}{2}Br_2(g) \rightarrow Cs_{1-x}PbBr_3^{(surf)} \cdots RNH_3^+ + CsBr^{(bulk)}$$

where R is CH_3- or $CH_3(CH_2)_3$-. The binding energy for methylammonium substitution is -3.98 eV, while the binding energy for butylammonium substitution is -4.13 eV. Ammonium substitution in the Cs vacancy operates through the formation of multiple H---Br hydrogen bonds. For methylammonium substitution, the H---Br lengths with the surface and subsurface Br atoms are around 2.320 Å and 2.861 Å respectively. For butylammonium substitution, the corresponding H---Br lengths are 2.353 Å and 2.856 Å. Hence, in this case as well, the geometry of the ammonium group in the Cs vacancy remains the same. Also, the orientation of the C-N bond with respect to the slab surface shows no appreciable variation (42.1º for methylammonium, 44.4º for butylammonium).

The difference in the binding energy for different ligand lengths can be due to Van der Waal's interactions of the ligand backbone with the slab surface, or due to lateral interactions between periodic images of the ligands, while the binding of the functional group (which is the primary subject of interest) remains the same. Thus, the ligands can be truncated to a single carbon without affecting the binding mechanism of the functional group.

Binding Energy Calculations

The determination of optimal slab thickness and ligand chain length was used to conduct ligand-binding studies on the (010) and (101) slabs with CsBr and $PbBr_2$ terminations. The possible ligand-binding mechanisms are listed below with the chemical reactions alongside [46]:

(i) MA adsorption:

$$CH_3NH_2(g) + CsPbBr_3^{(surf)} + \frac{1}{2}H_2(g) \rightarrow CsPbBr_3^{(surf)} \cdots CH_3NH_3^+$$

(ii) MA substitution in Cs vacancy (only on CsBr terminations):

$$CH_3NH_2(g) + CsPbBr_3^{(surf)} + \frac{1}{2}H_2(g) + \frac{1}{2}Br_2(g) \rightarrow$$

$$Cs_{1-x}PbBr_3^{(surf)} \cdots CH_3NH_3^+ + CsBr^{(bulk)}$$

(iii) OAc adsorption:

$$CH_3COOH(g) + CsPbBr_3^{(surf)} \rightarrow CsPbBr_3^{(surf)} \cdots CH_3COO^- + \frac{1}{2}H_2(g)$$

(iv) OAc substitution in Br vacancy:

$$CH_3COOH(g) + CsPbBr_3^{(surf)} \rightarrow CsPbBr_{3-x}^{(surf)} \cdots CH_3COO^- + \frac{1}{2}H_2(g) + \frac{1}{2}Br_2(g)$$

Geometry optimization was performed for each of these possible binding mechanisms and the ligand binding energies were calculated, which have been tabulated below in Table 3. An exhaustive set of calculations were performed considering all possible binding sites of each type available on the slab surface.

Table 3: Binding energies for individual ligands in different binding modes (most stable conformations shown for each case)

	1×1 (101) Surface		
		Adsorption	Substitution
CsBr	MA^+	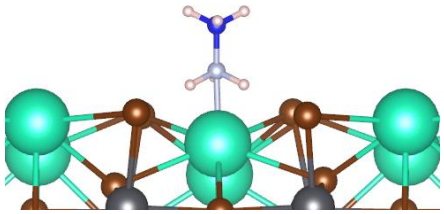 ΔE = 0.38 eV	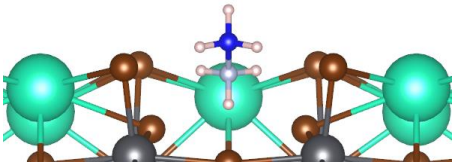 ΔE = -3.98 eV
	OAc^-	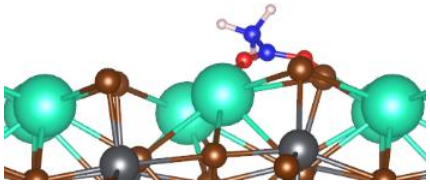 ΔE = 1.11 eV	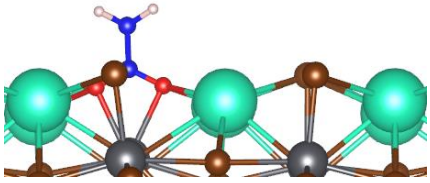 ΔE = 0.91 eV
$PbBr_2$	MA^+	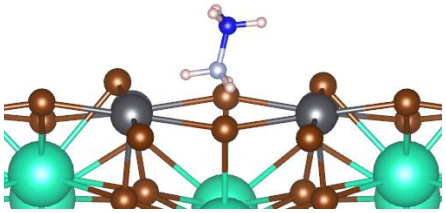 ΔE = -0.35 eV	-
	OAc^-	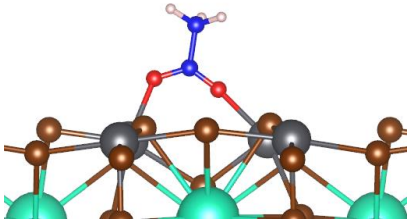 ΔE = 1.26 eV	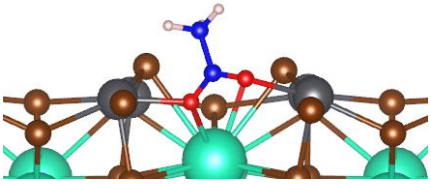 ΔE = 0.87 eV

	1×1 (010) Surface		
		Adsorption	Substitution
CsBr	MA^+	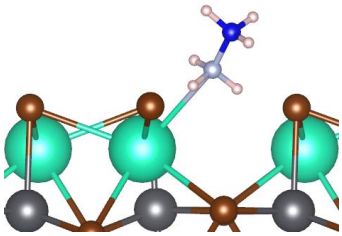 ΔE = 0.90 eV	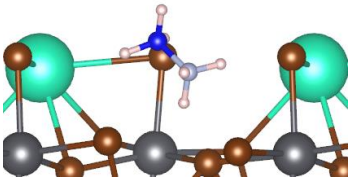 ΔE = -3.97 eV
	OAc^-	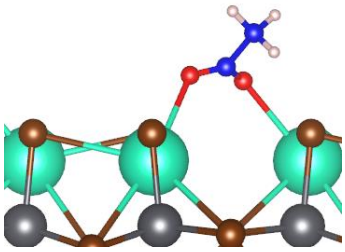 ΔE = 1.37 eV	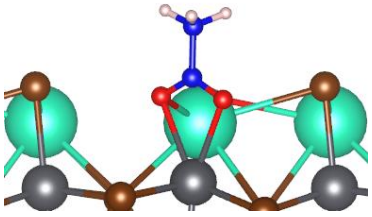 ΔE = 0.68 eV
$PbBr_2$	MA^+	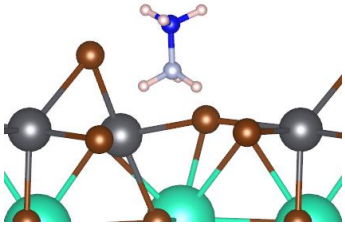 ΔE = -0.26 eV	-
	OAc^-	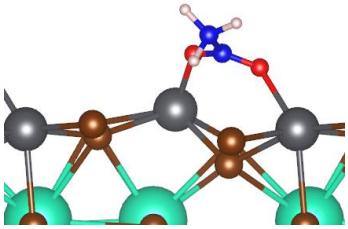 ΔE = 0.98 eV	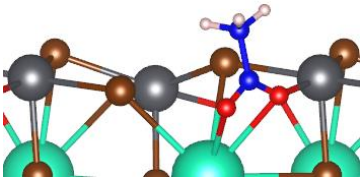 ΔE = 0.89 eV

<u>MA substitution in Cs vacancy</u>: To simulate methylammonium substitution in Cs vacancies, Cs atoms were removed from the CsBr-terminated surfaces and replaced with methylammonium ligands such that the N occupied the previous Cs position. This is the most thermodynamically favorable binding conformation (ΔE of -3.98 eV) on CsBr terminations, which is also reported in [46]. Stabilization of this conformation occurs through the formation of three H---Br H-bonds between the ammonium moiety and the surface Br atoms, which are

in the range of 2.350 Å to 2.850 Å, without a large disruption in the surface geometry relative to the clean slab. Cationic substitution on $PbBr_2$ surfaces is not feasible due to the resulting formation of charged surfaces which is highly unfavorable thermodynamically.

MA adsorption: The adsorption sites chosen for methylammonium were spaces surrounded by three surface Br atoms. Methylammonium adsorption is more favorable on the $PbBr_2$ surface (ΔE of -0.35 eV) compared to the CsBr surface. This is primarily because of the availability of triple H-bonding sites on the $PbBr_2$ surface without Cs ions that repel the positively charged ammonium moiety. The stabilization mechanism operates through the formation of H-bonds between the ammonium ^{1}H's and the surface Br atoms that are around 2.260 Å.

OAc substitution in Br vacancy: Acetate substitution was simulated by removing surface Br atoms and replacing them with acetate ligands such that the carboxylate group occupied the previous Br position. Acetate substitution in the Br vacancy has been studied for both CsBr and $PbBr_2$ terminations, out of which the CsBr termination is more amenable to this binding mechanism as evidenced by the binding energies in Table 3. The acetate ligand penetrates into the surface and coordinates with not only the surface cations, but also with subsurface cations through metal-oxygen bonds whose lengths are in the range 2.640 Å to 3.270 Å.

OAc adsorption: Adsorption of acetate was studied by bridging the carboxylate group using the O atoms across the surface cations, namely Cs for the CsBr terminations and Pb for the $PbBr_2$ terminations. This is the most thermodynamically unfavorable ligand binding configuration. Even though the carboxylate bridge across the surface cations is retained after geometry optimization, the acetate ligand is pushed away, hence making interactions with the subsurface cations virtually impossible.

It must be remembered that these calculations are performed at 0 K, hence the energetics have no entropic contributions. Also, the presence of a ligand shell around the PNCs can affect the ligand stabilization energies which is not accounted for in these calculations. This is because simulating a ligand layer over the slab surface would require the addition of a very large number of atoms and would make the calculations prohibitively expensive. Thus, the calculated binding energies should be used for comparison primarily, instead of determining the presence or absence of a particular binding mode.

Interpretation of NMR Results: ^{1}H-^{133}Cs CP-HETCOR

^{1}H-^{133}Cs CP-HETCOR (Figure 19) provides experimental information of the proximity between the ligands and the PNC surface. The Cs substitution model can be used to analyze the correlation with the ammonium ^{1}H's in the CP-HETCOR spectrum. As Cs substitution by the ammonium ligand is highly favorable, it can be expected that a lot of the Cs atoms are absent from the surface, which would be responsible for the low intensity of the surface Cs – ammonium ^{1}H cross peak. The distance between the ammonium ^{1}H's and subsurface Cs is in the range of 4.520 Å to 5.240 Å and hence is amenable for dipolar coupling to appear. This explains the strong correlation of the ammonium ^{1}H's with the Cs signal around 100 ppm, as the subsurface ^{133}Cs signal lies around 95 ppm. The distance between the ammonium ^{1}H's and subsurface Cs in case of methylammonium adsorption on the $PbBr_2$ surface is around 4.270 Å, which can be another source of contribution to the strong correlation of the ammonium ^{1}H's with the Cs signal around 100 ppm.

For acetate substitution in Br vacancies, the acetate ligand tilts on the surface in a manner which brings the alpha CH_2 group closer to the surface Cs atoms, resulting in alpha ^{1}H – surface Cs distances in the range 3.320 Å to 5.240 Å, contributing to the aliphatic ^{1}H – surface ^{133}Cs cross peak. The correlation between the aliphatic ^{1}H's and ^{133}Cs around 100 ppm can be understood through the model for acetate substitution in the Br vacancy on the $PbBr_2$ surface, where the distance between the alpha ^{1}H and the subsurface Cs is in the range 4.830 Å to 5.510 Å.

Co-substitution of Ligands

Calculations for ligand co-substitution were performed on the CsBr termination to understand the mechanism of the ion-pairing effect as evidenced by the ^{13}C-^{15}N TEDOR results. The models were constructed by removing a pair of nearest neighbor Cs and Br atoms from the surface and substituting them with the methylammonium and acetate ligands respectively. The binding energy results have been tabulated in Table 4.

On the (101) CsBr termination, co-substitution proved to be more stable than the sum of individual ligand substitutions by 0.12 eV. This can be ascribed to the formation of a H-bond between an ammonium ^{1}H and acetate oxygen, the bond length being 1.735 Å. Similar H-bond lengths were observed for the (010) CsBr termination as well. However, co-substitution was found to be more unstable than the sum of individual ligand substitutions. This could be due to increase in surface rumpling especially with the high substitution density on the 1×1 (010) slab,

as 1 out of every 2 Cs and Br atoms were being substituted. The surface rumpling effect may be decreased by substituting Cs-Br pairs on a supercell with larger transverse dimensions.

Table 4: Ligand co-substitution on CsBr-terminated surface

(101) Termination	(010) Termination
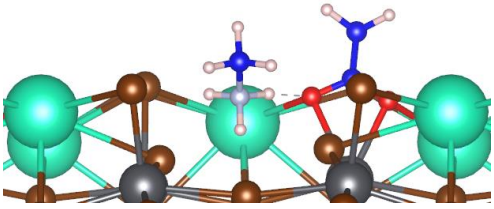 ΔE = -3.19 eV	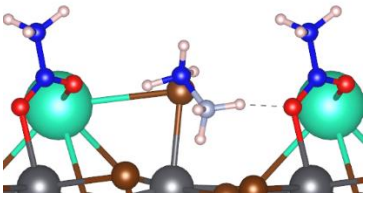 ΔE = -2.79 eV 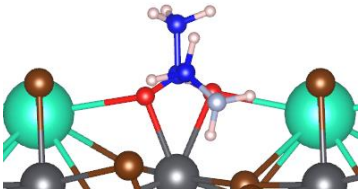 ΔE = -3.05 eV

The co-substitution calculations also showed that the distance between carboxylate C and ammonium N is in the range of 3.610 Å to 3.820 Å, which agrees excellently with the experimental estimation of the C-N distance between ligand pairs using TEDOR (Figure 23) as well as previous DFT studies with zwitterionic ligands [39].

(E) DFT CALCULATIONS OF NMR CHEMICAL SHIFTS

Computational Details

Theoretical calculations for chemical shifts of the various atomic nuclei in the composite systems can provide an enhanced understanding of the NMR spectra. For this purpose, GIPAW calculations have been performed on the relaxed models. The GIPAW pseudopotentials for the ligand nuclei, namely H, C, N and O, were generated using parameters taken from PSlibrary [74]. The all-electron wave functions and pseudo wavefunctions obtained from atomic calculations were compared to test the goodness of pseudization. The kinetic energy cutoffs used for wave function and electron density were 100 Ry and 600 Ry respectively.

The calibration references used for ^{13}C were adamantane (crystal structure taken from Crystallography Open Database entry 9013391, chemical shift taken from [70]), glycine (crystal structure taken from Crystallography Open Database entry 4504969, chemical shift taken from [72]), and histidine (crystal structure taken from Cambridge Structural Database deposition number 1176648, chemical shift taken from [71]). The calibration references used

for ^{15}N were glycine, histidine, and ammonium chloride (crystal structure taken from Materials Project entry 34337, chemical shift taken from [75]).

Chemical Shift Calibration

The shielding constants generated from a GIPAW calculation are not the experimental chemical shifts, but they instead must be shifted and scaled to match. This linear calibration of the calculated shielding constants is performed on reference systems with known crystal structures [51]. To test the effect of geometry optimization on the chemical shifts, GIPAW calculations were performed on a series of crystal structures for each of the reference systems. The series was composed of the following: unoptimized crystal structures, crystal structures optimized with the GIPAW pseudopotentials, and crystal structures optimized with the ultrasoft PBE-GGA pseudopotentials that were used for the ligand binding calculations in section (D). Both the unit cell parameters and the atomic positions were optimized, which is termed as variable cell relaxation. The effect of using a lower kinetic energy cutoff for the wavefunction, namely 60 Ry, was tested as well.

The GIPAW calculations do not show a significant variation in the calculated shielding constants upon changing the kinetic energy cutoff for the wavefunction, as the differences are less than 1 ppm. However, the choice of crystal structure used does affect the calculated shielding constants and calibration results to an appreciable extent. The relaxed structures show better calibration results in terms of the goodness of fit, especially for ^{15}N. The choice of pseudopotential used for the geometry optimization does not have an appreciable effect on the calculated shielding constants and calibration results. The improved agreement between calculated shielding constants and experimental chemical shifts upon geometry optimization corroborates previous studies in this regard [76]. Calibration parameters (Figure 27) obtained with crystal structures optimized using the ultrasoft PBE-GGA pseudopotentials were used to compute the chemical shifts for the ligand nuclei in the composite models.

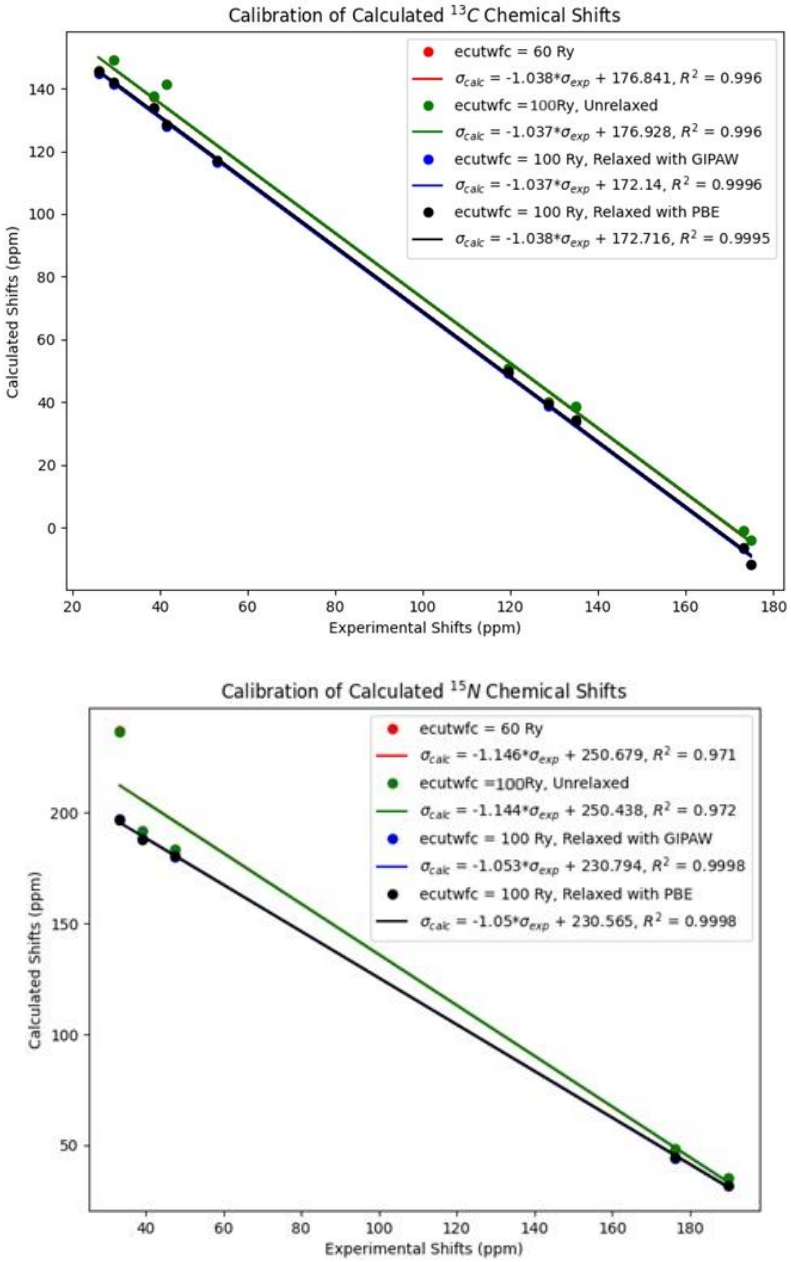

Figure 27: Calibration of calculated chemical shifts for ^{13}C (top) and ^{15}N (bottom)

Chemical Shift Calculations

GIPAW calculations were performed on the thermodynamically favorable binding composites. The chemical shifts have been tabulated below in Table 5. When compared to the ^{15}N CP profile at 100 K (Figure 17), the shoulder closely corresponds to the chemical shift obtained from methylammonium substitution in a Cs vacancy on the CsBr termination, while the main peak corresponds to the chemical shift obtained from methylammonium adsorption on the $PbBr_2$ termination. Similar ^{15}N chemical shifts are obtained for co-substitution of the methylammonium and acetate on the CsBr termination. The calculated ^{13}C chemical shifts for the carboxylate carbon also fall in the window of the TEDOR cross peak (Figure 22). These

chemical shifts combined with the C-N internuclear distance between the carboxylate and ammonium groups show that the TEDOR cross-peak contains contributions from ligand co-substitution, which provides additional support to the experimental evidence for cooperative ligand binding on the perovskite surface.

Table 5: Calculation of chemical shifts for thermodynamically favourable binding modes

	(101) Surface	(010) Surface
CsBr – Cs substitution by MA	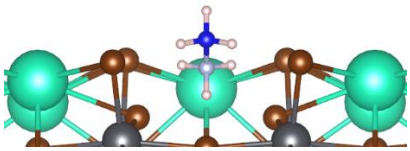 ^{15}N = 39.22 ppm	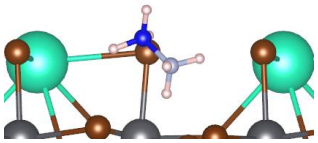 ^{15}N = 38.34 ppm
CsBr – Co-substition	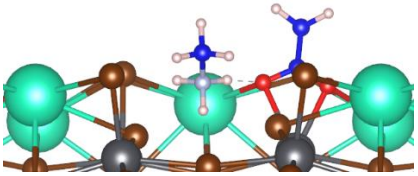 ^{15}N = 35.89 ppm, $^{13}C'$ = 181.79 ppm	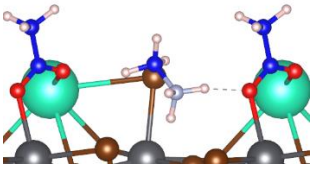 ^{15}N = 36.95 ppm, $^{13}C'$ = 172.33 ppm 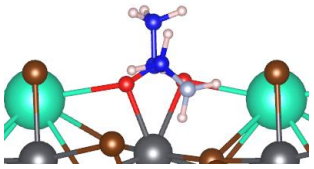 ^{15}N = 37.56 ppm, $^{13}C'$ = 179.59 ppm
$PbBr_2$ – MA adsorption	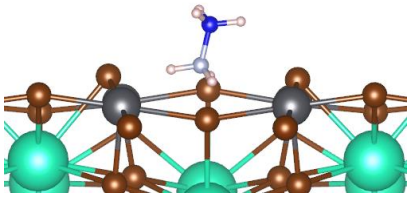 ^{15}N = 38.34 ppm	-

One ligand interaction mechanism that has not been considered in this DFT-based analysis for the TEDOR cross peak is the ligand shell. An ordered ligand shell composed of the acid and amine surfactants would show up in the TEDOR cross peak, but this cannot be studied by DFT with the information we possess. Further information such as distances between nearest neighbor acid and amine pairs, which can be obtained from homonuclear recoupling experiments analogous to TEDOR, would be required to construct the ligand shell model for DFT calculations.

CONCLUSION AND OUTLOOK

This study shows that the surface chemistry of colloidal $CsPbBr_3$ PNCs can be determined through solid-state NMR techniques complemented by signal enhancement with DNP. Both oleic acid and dodecylamine ligands have been observed to interact with the PNC surface, with dodecylamine being in excess as evidenced through NMR quantification. Dodecylamine in the protonated state binds to the PNC surface in a variety of ways, which is represented through the features in the 100 K ^{15}N spectrum that have been explained by DFT calculations. The amine binding modes include substitution of the ammonium group in Cs vacancies on CsBr-terminated surfaces, as well as adsorption on $PbBr_2$-terminated surfaces mediated through H-bonding with surface Br atoms. Different Cs species in the PNCs and their interactions with the ligands have been investigated through two-dimensional ^{1}H-^{133}Cs correlation techniques. Plausible explanations for the correlations of the ligands with the surface and subsurface Cs atoms have been provided using ammonium substitution in Cs vacancies and ammonium adsorption, as well as carboxylate substitution in Br vacancies. The first reported experimental verification and quantification of ligand proximity has been achieved through two-dimensional ^{1}H-^{13}C and ^{15}N-^{13}C correlation techniques, the latter experiment possible only through the use of DNP enhancement at 30 K. The correlation between the carboxylate carbon of oleic acid and ammonium nitrogen of dodecylamine has been analyzed with spin dynamics simulations to reveal an internuclear distance of 3.8 Å, which is corroborated by DFT calculations of ligand co-substitution on CsBr terminations. The co-substitution mechanism operates through the formation of H-bonds between the carboxylate and ammonium groups. Chemical shift calculations of the corresponding nuclei in ligand co-substitution models agreed with the experimental NMR spectra, providing further evidence for cooperative ligand-binding through this mechanism. In summary, this study has led to the establishment of a framework where proposed ligand-binding mechanisms on PNC surfaces can be studied and characterized at an atomic level through surface-specific solid-state NMR techniques complemented by *ab initio* theoretical studies of model systems.

The framework described and methods used in this study can be applied to the investigation and improvement of the different steps of PNC preparation. The synthesis step can be studied by observing the effects of varying precursor concentrations on the NMR spectra of PNC nuclei such as ^{133}Cs and identification of different atomic species, followed by the use of tailored solid-state NMR experiments to characterize the effects. The interaction of the PNC surface

with both native ligands and ligands used for exchange can be performed through correlation experiments as described in this study using nuclei that can be specifically ascribed to the individual ligands, such as ^{15}N for amines and ^{31}P for phosphonates. Also, ligand exchange can be quantified through comparison of one-dimensional quantitative spectra to understand the exchange thermodynamics. Additionally, modification and improvement of purification protocols such as washing can be done by studying the effect of these procedures on NMR spectra of both PNC and ligand atomic species. Solid-state NMR techniques are extremely versatile and can be extended to study a variety of PNC systems simply by modifying the NMR probe electronics to tune to the nuclei of interest. Lead-free perovskites such as $Cs_3Bi_2Br_9$ and Cs_2AgBiX_6 have proven to be an environment-friendly alternative to $APbX_3$ type perovskites. An important application of lead-free PNCs is the photoelectrocatalytic reduction of CO_2 [77]. The limited stability of these systems, especially in polar solvents, necessitates the use of strongly-binding zwitterionic ligands [36]. The framework for the investigation of the PNC surface as developed in this study will be essential for intelligent ligand design and ligand engineering in these systems.

Atomic-level characterization of the PNC surface chemistry as described in this study has opened up a way to validate results of DFT calculations and build improved DFT models with geometrical parameters obtained experimentally. This is essential, as blind DFT calculations for a large number of models is unnecessarily expensive, especially when a lot of the models can be discarded by considering experimental results. The NMR-validated DFT structures can be used to perform molecular dynamics simulations [78] to understand the interactions of the system with solvents and hence gain a clearer picture of the ligand equilibrium that governs the colloidal stability of PNCs as well as other kinds of quantum dots.

REFERENCES

[1] H. L. Wells, *Über die Cäsium- und Kalium-Bleihalogenide*, Z. Anorg. Chemie. **3**, 195 (1893).

[2] J. S. Manser, J. A. Christians, P. V. Kamat, *Intriguing Optoelectronic Properties of Metal Halide Perovskites*, Chem. Rev. **116**, 12956 (2016).

[3] V. D'Innocenzo, A. R. S. Kandada, M. De Bastiani, M. Gandini, and A. Petrozza, *Tuning the Light Emission Properties by Band Gap Engineering in Hybrid Lead Halide Perovskite*, J. Am. Chem. Soc. **136**, 17730 (2014).

[4] J. Liu, Y. He, L. Ding, H. Zhang, Q. Li, L. Jia, J. Yu, T. W. Lau, M. Li, Y. Qin, X. Gu, F. Zhang, Q. Li, Y. Yang, S. Zhao, X. Wu, J. Liu, T. Liu, Y. Gao, Y. Wang, X. Dong, H. Chen, P. Li, T. Zhou, M. Yang, X. Ru, F. Peng, S. Yin, M. Qu, D. Zhao, Z. Zhao, M. Li, P. Guo, H. Yan, C. Xiao, P. Xiao, J. Yin, X. Zhang, Z. Li, B. He, X. Xu, *Perovskite-silicon tandem solar cells with bilayer surface passivation*, Nature (2024).

[5] Y. Tian, C. Zhou, M. Worku, X. Wang, Y. Ling, H. Gao, Y. Zhou, Y. Miao, J. Guan, B. Ma, *Highly efficient spectrally stable red perovskite light-emitting diodes*, Adv. Mater. **30**, 1707093 (2018).

[6] Q. Zhang, Q. Shang, R. Su, T. T. H. Do, Q. Xiong, *Halide Perovskite Semiconductor Lasers: Materials, Cavity Design, and Low Threshold*, Nano Lett. **21**, 1903 (2021).

[7] D. W. deQuilettes, S. M. Vorpahl, S. D. Stranks, H. Nagaoka, G. E. Eperon, M. E. Ziffer, H. J. Snaith, D. S. Ginger, *Impact of microstructure on local carrier lifetime in perovskite solar cells*, Science **348**, 683 (2015).

[8] L. C. Schmidt, A. Pertegás, S. González-Carrero, O. Malinkiewicz, S. Agouram, G. M. Espallargas, H. J. Bolink, R. E. Galian, J. Pérez-Prieto, *Nontemplate Synthesis of $CH_3NH_3PbBr_3$ Perovskite Nanoparticles*, J. Am. Chem. Soc. **136**, 850 (2014).

[9] L. Protesescu, S. Yakunin, M. L. Bodnarchuk, F. Krieg, R. Caputo, C. H. Hendon, R. Xi Yang, A. Walsh, M. V. Kovalenko, *Nanocrystals of Cesium Lead Halide Perovskites ($CsPbX_3$, X = Cl, Br, and I): Novel Optoelectronic Materials Showing Bright Emission with Wide Color Gamut*, Nano Lett. **15**, 3692 (2015).

[10] J. V. Williams, N. A. Kotov, P. E. Savage, *A Rapid Hot-Injection Method for the Improved Hydrothermal Synthesis of CdSe Nanoparticles*, Ind. Eng. Chem. Res. **48**, 4316 (2009).

[11] Q. A. Akkerman, S. Park, E. Radichhi, F. Nunzi, E. Mosconi, F. De Angelis, R. Brescia, P. Rastogi, M. Prato, L. Manna, *Nearly Monodisperse Insulator Cs_4PbX_6 (X = Cl, Br, I) Nanocrystals, Their Mixed Halide Compositions, and Their Transformation into $CsPbX_3$ Nanocrystals*, Nano Lett. **17**, 1924 (2017).

[12] C. Han, C. Li, Z. Zang, M. Wang, K. Sun, X. Tang, J. Du, *Tunable luminescent $CsPb_2Br_5$ nanoplatelets: applications in light-emitting diodes and photodetectors*, Photonics Res. **5**, 473 (2017).

[13] D. Zhang, Y. Yang, Y. Bekenstein, Y. Yu, N. A. Gibson, A. B. Wong, S. W. Eaton, N. Kornienko, Q. Kong, M. Lai, A. P. Alivisatos, S. R. Leone, P. Yang, *Synthesis of Composition Tunable and Highly Luminescent Cesium Lead Halide Nanowires through Anion-Exchange Reactions*, J. Am. Chem. Soc. **138**, 7236 (2016).

[14] J. Shamsi, Z. Dang, P. Bianchini, C. Canale, F. Di Stasio, R. Brescia, M. Prato, L. Manna, *Colloidal Synthesis of Quantum Confined Single Crystal $CsPbBr_3$ Nanosheets with Lateral Size Control up to the Micrometer Range*, J. Am. Chem. Soc. **138**, 7240 (2016).

[15] P. Liu, W. Chen, W. Wang, B. Xu, D. Wu, J. Hao, W. Cao, F. Fang, Y. Li, Y. Zeng, R. Pan, S. Chen, W. Cao, X. Wei Sun, K. Wang, *Halide-Rich Synthesized Cesium Lead Bromide Perovskite Nanocrystals for Light-Emitting Diodes with Improved Performance*, Chem. Mater. **29**, 5168 (2017).

[16] M. Imran, V. Caligiuri, M. Wang, L. Goldoni, M. Prato, R. Krahne, L. De Trizio, L. Manna, *Benzoyl Halides as Alternative Precursors for the Colloidal Synthesis of Lead-Based Halide Perovskite Nanocrystals*, J. Am. Chem. Soc. **140**, 2656 (2018).

[17] S. E. Creutz, E. N. Crites, M. C. De Siena, D. R. Gamelin, *Colloidal Nanocrystals of Lead-Free Double-Perovskite (Elpasolite) Semiconductors: Synthesis and Anion Exchange To Access New Materials*, Nano Lett. **18**, 1118 (2018).

[18] X. Li, Y. Wu, S. Zhang, B. Cai, Y. Gu, J. Song, H. Zeng, *$CsPbX_3$ Quantum Dots for Lighting and Displays: Room-Temperature Synthesis, Photoluminescence Superiorities, Underlying Origins and White Light-Emitting Diodes*, Adv. Funct. Mater. **26**, 2435 (2016).

[19] Q. A. Akkerman, T. P. T. Nguyen, S. C. Boehme, F. Montanarella, D. N. Dirin, P. Wechsler, F. Beiglblöck, G. Rainò, R. Erni, C. Katan, J. Even, M. V. Kovalenko, *Controlling the nucleation and growth kinetics of lead halide perovskite quantum dots*, Science **377**, 1406 (2022).

[20] B. T. Diroll, G. Nedelcu, M. V. Kovalenko, R. D. Schaller, *High-Temperature Photoluminescence of $CsPbX_3$ (X = Cl, Br, I) Nanocrystals*, Adv. Funct. Mater. **27**, 1606750 (2017).

[21] G.C. La Rocca, *Wannier-Mott Excitons in Semiconductors, Thin Films and Nanostructures* **31**, 97 (Academic Press, 2003).

[22] J. Kang, L. Wang, *High Defect Tolerance in Lead Halide Perovskite $CsPbBr_3$*, J. Phys. Chem. Lett. **8**, 489 (2017).

[23] S. ten Brinck, F. Zaccaria, I. Infante, *Defects in Lead Halide Perovskite Nanocrystals: Analogies and (Many) Differences with the Bulk*, ACS Energy Lett. **4**, 2739 (2019).

[24] S. Huang, Z. Li, B. Wang, N. Zhu, C. Zhang, L. Kong, Q. Zhang, A. Shan, L. Li, *Morphology Evolution and Degradation of $CsPbBr_3$ Nanocrystals under Blue Light-Emitting Diode Illumination*, ACS Appl. Mater. Interfaces **9**, 7249 (2017).

[25] Y. Yang, Y. Chen, C. Hou, T. Liang, *Ground-State Surface of All-Inorganic Halide Perovskites*, J. Phys. Chem. C **126**, 21155 (2022).

[26] K. Fausia, B. Nharangatt, R. N. Vinayakan, A. R. Ramesh, V. Santhi, K. R. Dhandapani, T. P. Manoj, R. Chatanathodi, D. Jose, K. Sandeep, *Probing the Structural Degradation of $CsPbBr_3$ Perovskite Nanocrystals in the Presence of H_2O and H_2S: How Weak Interactions and HSAB Matter*, ACS Omega **9**, 8417 (2024).

[27] Y. Sun, H. Zhang, K. Zhu, W. Ye, L. She, X. Gao, W. Ji, Q. Zeng, *Research on the influence of polar solvents on $CsPbBr_3$ perovskite QDs*, RSC Adv. **11**, 27333 (2021).

[28] J. De Roo, M. Ibáñez, P. Geiregat, G. Nedelcu, W. Walravens, J. Maes, J. C. Martins, I. V. Driessche, M. V. Kovalenko, Z. Hens, *Highly Dynamic Ligand Binding and Light Absorption Coefficient of Cesium Lead Bromide Perovskite Nanocrystals*, ACS Nano **10**, 2071 (2016).

[29] M. L. H. Green, G. Parkin, *Application of the Covalent Bond Classification Method for the Teaching of Inorganic Chemistry*, J. Chem. Educ. **91**, 807 (2014).

[30] A. Heuer-Jungemann, N. Feliu, I. Bakaimi, M. Hamaly, A. Alkilany, I. Chakraborty, A. Masood, M. F. Casula, A. Kostopoulou, E. Oh, K. Susumu, M. H. Stewart, I. L. Medintz, E. Stratakis, W. J. Parak, A. G. Kanaras, *The Role of Ligands in the Chemical Synthesis and Applications of Inorganic Nanoparticles*, Chem. Rev. **119**, 4819 (2019).

[31] M. Imran, P. Ijaz, D. Baranov, L. Goldoni, U. Petralanda, Q. Akkerman, A. L. Abdelhady, M. Prato, P. Bianchini, I. Infante, L. Manna, *Shape-Pure, Nearly Monodispersed $CsPbBr_3$ Nanocubes Prepared Using Secondary Aliphatic Amines*, Nano Lett. **18**, 7822 (2018).

[32] B. Zhang, L. Goldoni, C. Lambruschini, L. Moni, M. Imran, A. Pianetti, V. Pinchetti, S. Brovelli, L. De Trizio, L. Manna, *Stable and Size Tunable $CsPbBr_3$ Nanocrystals Synthesized with Oleylphosphonic Acid*, Nano Lett. **20**, 8847 (2020).

[33] S. R. Smock, T. J. Williams, R. L. Brutchey, *Quantifying the Thermodynamics of Ligand Binding to $CsPbBr_3$ Quantum Dots*, Angew. Chem. Int. Ed. **57**, 11711 (2018).

[34] M. Imran, P. Ijaz, L. Goldoni, D. Maggioni, U. Petralanda, M. Prato, G. Almeida, I. Infante, L. Manna, *Simultaneous Cationic and Anionic Ligand Exchange for Colloidally Stable $CsPbBr_3$ Nanocrystals*, ACS Energy Lett. **4**, 819 (2019).

[35] F. Krieg, S. T. Ochsenbein, S. Yakunin, S. ten Brinck, P. Aellen, A. Süess, B. Clerc, D. Guggisberg, O. Nazarenko, Y. Shynkarenko, S. Kumar, C. Shih, I. Infante, M. V. Kovalenko, *Colloidal $CsPbX_3$ (X = Cl, Br, I) Nanocrystals 2.0: Zwitterionic Capping Ligands for Improved Durability and Stability*, ACS Energy Lett. **3**, 641 (2018).

[36] V. Morad, A. Stelmakh, M. Svyrydenko, L. G. Feld, S. C. Boehme, M. Aebli, J. Affolter, C. J. Kaul, N. J. Schrenker, S. Bals, Y. Sahin, D. N. Dirin, I. Cherniukh, G. Raino, A. Baumketner, M. V. Kovalenko, *Designer phospholipid capping ligands for soft metal halide nanocrystals*, Nature **626**, 542 (2024).

[37] C. F. Holder, R. E. Schaak, *Tutorial on Powder X-ray Diffraction for Characterizing Nanoscale Materials*, ACS Nano **13**, 7359 (2019).

[38] H. Jensen, J. H. Pedersen, J. E. Jørgensen, J. S. Pedersen, K. D. Joensen, S. B. Iversen, E. G. Søgaard, *Determination of size distributions in nanosized powders by TEM, XRD, and SAXS*, J. Exp. Nanosci. **1**, 355 (2006).

[39] H. Zhu, M. Kick, M. Ginterseder, C. J. Krajewska, T. Sverko, R. Li, Y. Lu, M. Shih, T. Van Voorhis, M. G. Bawendi, *Synthesis of Zwitterionic $CsPbBr_3$ Nanocrystals with Controlled Anisotropy using Surface-Selective Ligand Pairs*, Adv. Mater. **35**, 2304069 (2023).

[40] J. Liu, K. Song, Y. Shin, X. Liu, J. Chen, K. X. Yao, J. Pan, C. Yang, J. Yin, L. Xu, H. Yang, A. M. El-Zohry, B. Xin, S. Mitra, M. N. Hedhili, I. S. Roqan, O. F. Mohammed, Y. Han, O. M. Bakr, *Light-Induced Self-Assembly of Cubic $CsPbBr_3$ Perovskite Nanocrystals into Nanowires*, Chem. Mater. **31**, 6642 (2019).

[41] Z. Dang, J. Shamsi, F. Palazon, M. Imran, Q. A. Akkerman, S. Park, G. Bertoni, M. Prato, R. Brescia, L. Manna, *In Situ Transmission Electron Miscroscopy Study of Electron Beam-Induced Transformations in Colloidal Cesium Lead Halide Perovskite Nanocrystals*, ACS Nano **11**, 2124 (2017).

[42] T. Udayabhaskararao, M. Kazes, L. Houben, H. Lin, D. Oron, *Nucleation, Growth, and Structural Transformations of Perovskite Nanocrystals*, Chem. Mater. **29**, 1302 (2017).

[43] Y. Yu, D. Zhang, C. Kisielowski, L. Dou, N. Kornienko, Y. Bekenstein, A. B. Wong, A. P. Alivisatos, P. Yang, *Atomic Resolution Imaging of Halide Perovskites*, Nano Lett. **16**, 7530 (2016).

[44] A. Pan, B. He, X. Fan, Z. Liu, J. J. Urban, A. P. Alivisatos, L. He, Yi Liu, *Insight into the Ligand-Mediated Synthesis of Colloidal $CsPbBr_3$ Perovskite Nanocrystals: The Role of Organic Acid, Base, and Cesium Precursors*, ACS Nano **10**, 7943 (2016).

[45] M. A. Uddin, J. K. Mobley, A. A. Masud, T. Liu, R. L. Calabro, D. Kim, C. I. Richards, K. R. Graham, *Mechanistic Exploration of Dodecanethiol-Treated Colloidal $CsPbBr_3$ Nanocrystals with Photoluminescence Quantum Yields Reaching Near 100%*, J. Phys. Chem. **123**, 18103 (2019).

[46] V. K. Ravi, P. K. Santra, N. Joshi, J. Chugh, S. K. Singh, H. Rensmo, P. Ghosh, A. Nag, *Origin of the Substitution Mechanism for the Binding of Organic Ligands on the Surface of $CsPbBr_3$ Perovskite Nanocubes*, J. Phys. Chem. Lett. **8**, 4988 (2017).

[47] Q. Zhong, M. Cao, Y. Xu, P. Li, Y. Zhang, H. Hu, D. Yang, Y. Xu, L. Wang, Y. Li, X. Zhang, Q. Zhang, *L-Type Ligand-Assisted Acid-Free Synthesis of $CsPbBr_3$ Nanocrystals with*

Near-Unity Photoluminescence Quantum Yield and High Stability, Nano Lett. **19**, 4151 (2019).

[48] Z. Hens, J. C. Martins, *A Solution NMR Toolbox for Characterizing the Surface Chemistry of Colloidal Nanocrystals*, Chem. Mater. **25**, 1211 (2013).

[49] J. Yin, H. Yang, L. Gutiérrez-Arzaluz, Y. Zhou, J. Brédas, O. M. Bakr, O. F. Mohammed, *Luminescence and Stability Enhancement of Inorganic Perovskite Nanocrystals via Selective Surface Ligand Binding*, ACS Nano **15**, 17998 (2021).

[50] Y. Chen, S. R. Smock, A. H. Flintgruber, F. A. Perras, R. L. Brutchey, A. J. Rossini, *Surface Termination of $CsPbBr_3$ Perovskite Quantum Dots Determined by Solid-State NMR Spectroscopy*, J. Am. Chem. Soc. **142**, 6117 (2020).

[51] W. Cao, A. Yakimov, X. Qian, J. Li, X. Peng, X. Kong, C. Copéret, *Surface Sites and Ligation in Amine-capped CdSe Nanocrystals*, Angew. Chem. Int. Ed. **62**, e202312713 (2023).

[52] S. Badoni, M. Terlecki, S. Carret, J. Poisson, T. Charpentier, H. Okuno, M. Wolska-Pietkiewicz, D. Lee, J. Lewiński, G. De Paëpe, *Atomic-Level Structure of the Organic-Inorganic Interface of Colloidal ZnO Nanoplatelets from Dynamic Nuclear Polarization-Enhanced NMR*, J. Am. Chem. Soc. **146**, 27655 (2024).

[53] L. Piveteau, T. Ong, A. J. Rossini, L. Emsley, C. Copéret, M. V. Kovalenko, *Structure of Colloidal Quantum Dots from Dynamic Nuclear Polarization Surface Enhanced NMR Spectroscopy*, J. Am. Chem. Soc. **137**, 13964 (2015).

[54] A. Mishra, M. A. Hope, M. Almalki, L. Pfeifer, S. M. Zakeeruddin, M. Grätzel, L. Emsley, *Dynamic Nuclear Polarization Enables NMR of Surface Passivating Agents on Hybrid Perovskite Thin Films*, J. Am. Chem. Soc. **144**, 15175 (2022).

[55] A. Mishra, M. A. Hope, G. Stevenato, D. J. Kubicki, L. Emsley, *Dynamic Nuclear Polarization of Inorganic Halide Perovskites*, J. Phys. Chem. C **127**, 11094 (2023).

[56] S. Paul, E. Bouleau, Q. Reynard-Feytis, J. Arnaud, F. Bancel, B. Rollet, P. Dalban-Moreynas, C. Reiter, A. Purea, F. Engelke, S. Hediger, G. De Paëpe, *Sustainable and cost-effective MAS DNP-NMR at 30K with cryogenic sample exchange*, J. Magn. Reson. **356**, 10761 (2023).

[57] E. R. Andrew, A. Bradbury, R. G. Eades, *Nuclear Magnetic Resonance Spectra from a Crystal Rotated at High Speed*, Nature **182**, 1659 (1958).

[58] M. J. Duer, *Introduction to Solid-State NMR Spectroscopy* (Wiley-Blackwell, 2005).

[59] M. Bak, J. T. Rasmussen, N. C. Nielsen, *SIMPSON: A General Simulation Program for Solid-State NMR Spectroscopy*, J. Magn. Reson. **147**, 296 (2000).

[60] B. Corzilius, *Theory of solid effect and cross effect dynamic nuclear polarization with half-integer high-spin metal polarizing agents in rotating solids*, Phys. Chem. Chem. Phys. **18**, 27190 (2016).

[61] S. Hediger, D. Lee, F. Mentink-Vigier, G. De Paëpe, *MAS-DNP Enhancements: Hyperpolarization, Depolarization, and Absolute Sensitivity*, eMagRes **7**, 105 (2018).

[62] M. E. Halse, J. Schlagnitweit, L. Emsley, *High-Resolution ^{1}H Solid-State NMR Spectroscopy Using Windowed LG4 Homonuclear Dipolar Decoupling*, Isr. J. Chem. **54**, 136 (2014).

[63] T. Gullion, *Introduction to rotational-echo, double-resonance NMR*, Concepts Magn. Reson. **10**, 277 (1998).

[64] C. P. Jaroniec, B. A. Tounge, J. Herzfeld, R. G. Griffin, *Frequency Selective Heteronuclear Dipolar Recoupling in Rotating Solids: Accurate ^{13}C-^{15}N Distance Measurements in Uniformly ^{13}C, ^{15}N-labeled Peptides*, J. Am. Chem. Soc. **123**, 3507 (2001).

[65] C. P. Jaroniec, C. Filip, R. G. Griffin, *3D TEDOR NMR Experiments for the Simultaneous Measurement of Multiple Carbon-Nitrogen Distances in Uniformly ^{13}C, ^{15}N-labeled Peptides*, J. Am. Chem. Soc. **124**, 10728 (2002).

[66] D. S. Sholl, J. A. Steckel, *Density Functional Theory: A Practical Introduction* (Wiley, 2009).

[67] B. Meyer, D. Vanderbilt, *Ab initio study of $BaTiO_3$ and $PbTiO_3$ surfaces in external electric fields*, Phys. Rev. B **63**, 205426 (2001).

[68] C. J. Pickard, F. Mauri, *All-electron magnetic response with pseudopotentials: NMR chemical shifts*, Phys. Rev. B **63**, 245101 (2001).

[69] P. Giannozzi, S. Baroni, N. Bonini, M. Calandra, R. Car, C. Cavazzoni, D. Ceresoli, G. L. Chiarotti, M. Cococcioni, I. Dabo, A. Dal Corso, S. de Gironcoli, S. Fabris, G. Fratesi, R.

Gebauer, U. Gerstmann, C. Gougoussis, A. Kokalj, M. Lazzeri, L. Martin-Samos, N. Marzari, F. Mauri, R. Mazzarello, S. Paolini, A. Pasquarello, L. Paulatto, C. Sbraccia, S. Scandolo, G. Sclauzero, A. P. Seitsonen, A. Smogunov, P. Umari, R. M. Wentzcovitch, *QUANTUM ESPRESSO: a modular and open-source software project for quantum simulations of materials*, J. Phys.: Condens. Matter **21**, 395502 (2009).

[70] D. H. Brouwer, M. Horvath, *Minimizing the effects of RF inhomogeneity and phase transients allows resolution of two peaks in the ^{1}H CRAMPS NMR spectrum of adamantane*, Solid State Nucl. Magn. Reson. **71**, 30 (2015).

[71] S. Li, L. Zhou, Y. Su, B. Han, F. Deng, *^{13}C and ^{15}N spectral editing inside histidine imidazole ring through solid-state NMR spectroscopy*, Solid State Nucl. Magn. Reson. **54**, 13 (2013).

[72] M. Ghosh, N. Kango, K. K. Dey, *Investigation of the internal structure and dynamics of cellulose by ^{13}C-NMR relaxometry and 2DPASS-MAS-NMR measurements*, J. Biomol. NMR **73**, 601 (2019).

[73] T. J. N. Hooper, Y. Fang, A. A. M. Brown, S. H. Pu, T. J. White, *Structure and surface properties of size-tuneable $CsPbBr_3$ nanocrystals*, Nanoscale **13**, 15770 (2021).

[74] A. Dal Corso, *Pseudopotentials periodic table: From H to Pu*, Comput. Mater. Sci. **95**, 337 (2014).

[75] P. Bertani, J. Raya, B. Bechinger, *^{15}N chemical shift referencing in solid state NMR*, Solid State Nucl. Magn. Reson. **61-62**, 15 (2014).

[76] L. Szeleszczuk, D. M. Pisklak, M. Zielińska-Pisklak, *Does the Choice of the Crystal Structure Influence the Results of the Periodic DFT Calculations? A Case of Glycine Alpha Polymorph GIPAW NMR Parameters Computations*, J. Comput. Chem. **39**, 853 (2018).

[77] S. S. Bhosale, A. K. Kharade, E. Jokar, A. Fathi, S. Chang, E. W. Diau, *Mechanism of Photocatalytic CO_2 Reduction by Bismuth-Based Perovskite Nanocrystals at the Gas-Solid Interface*, J. Am. Chem. Soc. **141**, 20434 (2019).

[78] X. Wang, D. Toroz, S. Kim, S. L. Clegg, G. Park, D. Di Tommaso, *Density functional theory based molecular dynamics study of solution composition effects on the solvation shell of metal ions*, Phys. Chem. Chem. Phys. **22**, 16301 (2020).

[79] N. Yantara, S. Bhaumik, F. Yen, D. Sabba, H. A. Dewi, N. Mathews, P. P. Boix, H. V. Demir, S. Mhaisalkar, *Inorganic Halide Perovskites for Efficient Light-Emitting Diodes*, J. Phys. Chem. Lett. **6**, 4360 (2015).

[80] G. Metz, X. Wu, S. O. Smith, *Ramped-Amplitude Cross Polarization in Magic-Angle-Spinning NMR*, J. Magn. Reson. Series A **110**, 219 (1994).

[81] S. R. Hartmann, E. L. Hahn, *Nuclear Double Resonance in the Rotating Frame*, Phys. Rev. **128**, 2042 (1962).

[82] M . Lee, W. I. Goldburg, *Nuclear-Magnetic-Resonance Line Narrowing by a Rotating RF Field*, Phys. Rev. **140**, A1261 (1965).

[83] R. S. Thakur, N. D. Kurur, P. K. Madhu, *Swept-frequency two-pulse phase modulation for heteronuclear dipolar decoupling in solid-state NMR*, Chem. Phys. Lett. **426**, 459 (2006).

[84] C. Ye, R. Fu, J. Hu, L. Hou, S. Ding, *Carbon-13 chemical shift anisotropies of solid amino acids*, Magn. Reson. Chem. **31**, 699 (1993).

[85] A. Venkatesh, G. Casano, R. Wei, Y. Rao, H. Lingua, H. Karoui, M. Yulikov, O. Ouari, L. Emsley, *Rational Design of Dinitroxide Polarizing Agents for Dynamic Nuclear Polarization to Enhance Overall NMR Sensitivity*, Angew. Chem. Int. Ed. **63**, e202317337 (2024).

[86] P. Hohenberg, W. Kohn, *Inhomogeneous Electron Gas*, Phys. Rev. **136**, B864 (1964).

[87] W. Kohn, L. J. Sham, *Self-Consistent Equations Including Exchange and Correlation Effects*, Phys. Rev. **140**, A1133 (1965).

[88] K. P. Huber, G. Herzberg, *Molecular Spectra and Molecular Structure* (Springer New York, 2013).